Electronic Properties of Amorphous and Crystalline $Fe_xCo_{1-x}Zr_2$ Alloys

by

Maria Dikeakos

Center for the Physics of Materials
Department of Physics, McGill University
Montréal, Canada

March 1995

A Thesis submitted to the
Faculty of Graduate Studies and Research
in partial fulfillment of the requirements for the degree of
Master of Science

0-612-44086-9

to my cousin

Maria Rizakos

Abstract

The electronic contribution to the resistivity ρ and its temperature dependence were investigated for amorphous and crystalline $[Fe_xCo_{1-x}]_{33.3}Zr_{66.7}$ $(0 \leq x \leq 1)$ alloys in the temperature range 80-300 K. As Fe-rich compositions may exhibit spin fluctuation effects, transport properties were not studied below 80 K where spin fluctuation effects must be taken into consideration. The compositional and structural integrity of the samples was verified by means of X-ray diffractometry, electron-microprobe analysis, and differential scanning calorimetry. It was also confirmed that the first crystallization product for all the compositions is the face-centered cubic phase with the $NiTi_2$-type structure. A true comparison between amorphous and crystalline transport properties was thus possible. For the metallic glasses, it was observed that $\rho(T)$ had a temperature dependence of the form: $A + Bexp(-T/\Delta)$ in agreement with Mizutani who proposed this relation for glasses containing a significant number of d-electrons at E_F. The characteristic temperature, Δ, was found to be related to the Debye temperature, θ_D, and the parameter B to the electronic specific heat coefficient, γ. The resistivity data for the crystalline tenary compounds exhibited a $(c - bT + aT^2)$-dependence. Both the glasses and their crystalline counterparts were characterized by negative temperature coefficients of the resistivity, α. However, for the glasses, α increased as the Fe content increased whereas for the crystalline compounds α decreased as the Fe content increased.

Résumé

La contribution électronique à la résistivité ρ et sa dépendance en température ont été examinées pour les alliages amorphes et cristallins de $[Fe_xCo_{1-x}]_{33.3}Zr_{66.7}$ $(0 \leq x \leq 1)$ dans la gamme de température 80-300K. Puisque des effets de fluctuations de spin peuvent se manifester dans les compositions riches en fer, les propriétés de transport n'ont pas été étudiées au-dessous de 80 K là où ces effets de fluctuations de spin doivent être pris en considération. L'intégrité de la composition et de la structure des échantillons a été vérifiée au moyen de la diffraction des rayons X, de l'analyse par microsoude électronique, et de la calorimétrie différentielle. De plus, il a été confirmé que le premier produit de cristallisation de toutes ces compositions est la phase cubique face-centrée avec la structure de type $NiTi_2$. Une comparaison exacte entre les propriétés de transport des alliages amorphes et celles des alliages cristallins était ainsi possible. Pour les verres métalliques, on a observé que $\rho(T)$ avait une dépendance de la forme: $A + Bexp(-T/\Delta)$ conformément aux travaux de Mizutani qui a proposé cette relation pour des verres contenant un nombre significatif d'électrons d à E_F. Un lien a été établi entre la température caractéristique, Δ, et la température Debye, θ_D, ainsi que le paramètre B du coefficient électronique de la chaleur spécifique. Les données de résistivité pour les composés ternaires cristallins ont révelé une dépendance telle que $(c - bT + aT^2)$. Les verres métalliques et leurs pendants cristallins ont été caractérisés par des valeurs négatives des coefficients de la résistivité, α. Cependant, avec l'augmentation du contenu ferrique, α a augmenté pour les verres métalliques tandis que pour les composés cristallins α a diminué.

Acknowledgments

Throughout the many stages of this work, I received the help of many people whom I would now like to take the opportunity to thank.

Firstly, I would like to express my gratitude to my supervisor, Zaven Altounian, for his patience and guidance throughout my thesis work. His critical advice and instruction helped clarify much of the physics involved in this research.

The expertise of Ming Mao during the initial phase of this work was of immense value. He took the time to instruct me on how to use the melt-spinning apparatus and prepared the quartz tubes used in the process. Thanks to Ralf Brüning for his useful suggestions concerning the density measurements and the 'dreaded' DSC data transfer. Gratitude is owed to Glenn Poirier for his assistance with the electron microprobe analysis. Rita Koknaeva was always willing to answer any questions I may have had about X-ray diffractometry. I would like to thank her for her help with the structural analysis of some of the crystalline samples as well as for our countless enlightening discussions.

I would also like to thank Louis Taillefer for providing access to his laboratory and, most of all, his cryostat. Robert Gagnon's instructions on the use of the cryostat were greatly appreciated. Thanks also to Mohsen Sabouri-Ghomi for sharing his experience in mounting samples for the resistivity measurements. I am grateful to Sebastien Ricchi and Martin Lacasse for their 'eleventh hour' help with the exponential fits.

Kindly technical support was provided by John Egyed and Frank Van Gils. I would also like to thank the secretarial staff: Paula Domingues, Cynthia Lue-Yat, and Joanne Longo as well as the administrative officer, Diane Koziol. I am also grateful to Pascal Tessier for his help with the french translation of the abstract.

For making the last two years memorable, warm thanks to Rita Koknaeva, Dominique Pouliot, Louis Normand, David Binding, Kostas Kordas, Graham Cross, Niri Govind, François Drolet, Erol Girt, Patricia Silas, Pascal Tessier, Mohsen Sabouri-Ghomi, Andrew Dawson, Ou Mao, Yi Zhao, Chen Xin He, Eric Dufresne, Eugenia Corvera, Geoff Soga, Mikko Kartunnen, Marianna Ciureanu, Benoît Lussier, Denis Michaud and to my fellow sport buffs Stéphane Legault and Réjean Ducharme (S.F. 49'ers all the way!). I'm extremely grateful to Randa Abdouche and Nick Provatas for their advice, encouragement, and entertaining conversations.

A special thanks to Elizabeth Lai-Fook for her friendship and moral support.

Financial support was provided by a scholarship from the Fonds pour la Formation de Chercheurs et l'Aide à la Recherche (Québec).

I especially thank my family for their unwavering support along the way. Above all, I thank God for helping me see my way through the more difficult times.

Contents

List of Figures

List of Tables

Chapter 1

Introduction

The term "glass" is almost invariably associated with the traditional transparent and brittle window material and household glassware [1]. However, strictly speaking, a glass is a non-crystalline (i.e., amorphous) solid obtained by quenching a liquid.

The ability to form glasses varies for different materials. Silicate mixtures vitrify at slow cooling rates ($\approx 10^{-2}$ K/s) [2] and indeed are often hard to crystallize. Metallic glasses are considerably more difficult to produce and require very high cooling rates, in excess of 10^6 K/s [1]. If a liquid is cooled sufficiently rapid past the melting point T_m, the time and energy required for nucleation and growth of crystallites is inadequate and crystallization is bypassed. Thus, the liquid phase persists until a lower temperature T_g is reached. At T_g, the glass transition temperature, the supercooled liquid is effectively a solid because the time needed for configurational relaxation becomes too long on a laboratory time-scale [3]. Liquid-like structural disorder is frozen in the glassy solid.

Both liquid and amorphous alloys are characterized by the absence of long-range atomic order. However, unlike liquids, amorphous alloys do exhibit local correlation. Topological and chemical order exists for a few interatomic distances about any given atom. Thus, glasses seem to have this high degree of short-range order in common with crystals. In contrast though, the equilibrium positions of the atoms in crystalline solids form a translationally periodic array; long-range atomic order exists for crystals.

Owing to this structural difference, various physical, chemical, magnetic, and electronic properties of a metallic glass differ from those of crystalline materials [1,2,4]. Among these properties mention may be made of high hardness, exceptional mechanical strength, corrosion resistance surpassing that of stainless steel in many cases, easy magnetizability, electron localization effects at low temperatures (for most metallic glasses), high electrical resistivity and small temperature coefficient of resistivity which can be positive or negative.

The electron transport properties of amorphous materials have been a much explored subject for the past two decades. Several theories have been developed to explain their resistivity, ρ, at high as well as low temperatures [5]. One of the early theories was proposed by Faber and Ziman in 1965 [6]. It was based on the following assumptions:

- The glass is composed of rigidly fixed ions (nuclei and core electrons) with a nearly free electron gas consisting of valence electrons.
- The electron transport properties can be described in terms of the Boltzmann equation.
- Each ion interacts with the conduction electrons through a localized pseudopotential.
- The total effect of the ions is given by ordinary perturbation theory.

Unfortunately, actual resistivity measurements revealed that this assumption of electrons scattering elastically off ions was inadequate. As a result, a "generalized"

Faber-Ziman theory was constructed which incorporates electron-phonon interactions into the original theory [5].

The temperature dependence of the electrical resistivity arises from the interaction of conduction electrons with lattice vibrations [7]. At low temperatures, superconductivity and quantum interference effects come into play. The influence of the superconducting fluctuations on $\rho(T)$ above the critical temperature has been analyzed both theoretically [8–10] and experimentally [11,12]. A somewhat unusual resistivity behaviour occurs in nearly magnetic amorphous systems. This effect was systematically studied recently [13] in amorphous $Fe_xNi_{1-x}Zr_2$ and was attributed to the presence of spin fluctuations. It was established that the spin fluctuation contribution to the resistivity varies as T^2 at extremely low temperatures and as T at higher temperatures.

In this thesis, the electronic contribution to the resistivity and its temperature dependence are investigated for amorphous and crystalline $Fe_xCo_{1-x}Zr_2$ ($0 \leq x \leq 1$) alloys. A similar study was previously carried out on $Fe_xNi_{1-x}Zr_2$ ternary glasses [13]. However, in this earlier study, neither the temperature dependence of the resistivity nor the transport properties of the crystalline state were investigated. In both of these systems, the glassy structure remains basically the same since Fe, Co and Ni have essentially similar atomic sizes and only the electron density changes. In the $Fe_xNi_{1-x}Zr_2$ glassy system, only those compositions with $x > 0.4$ crystallize into the face-centered cubic (*fcc*) phase with the $NiTi_2$-type structure while the Ni-rich compositions crystallize into a body-centered tetragonal (*bct*) phase with the Al_2Cu structure. A comparison of the glassy and crystalline transport properties in such a system is therefore not ideal. Moreover, as mentioned above, spin-fluctuation effects will introduce non-linear contributions to the resistivities of the glassy alloys to various degrees depending on composition. In the $Fe_xCo_{1-x}Zr_2$ system, on the other hand, as the first crystallization product for $FeZr_2$ and $CoZr_2$ is the face-centered cubic phase with the $NiTi_2$-type structure all compositions should crystallize into this crystalline phase. It is expected, therefore, that a true comparison between amorphous and crystalline transport properties can be made over the entire composition range. Here, the intention was to crystallize the glass samples and compare the resistivity of the crystalline state with that of the amorphous state in the temperature range from 80 K to 300 K. As Fe-rich compositions may exhibit spin fluctuation effects, transport properties were not studied below 80 K where spin fluctuation effects must be taken into consideration. To ensure the required compositional and structural integrity of the alloys, great care was taken during their preparation and subsequent characterization. The amorphous samples were produced by rapid quenching of the melt. Their crystalline counterparts were prepared using a differential scanning calorimeter. Verification of the composition and phase of these pseudo-binary alloys was made using X-ray diffractometry, electron microprobe analysis, and differential scanning calorimetry. The actual low temperature resistivity was measured using a four-probe ac technique.

To summarize, the aim of this thesis is to prepare and characterize $Fe_xCo_{1-x}Zr_2$ metallic glasses. The samples should be free of crystalline phases either on the surface or as inclusions. The composition dependence of the crystallization characteristics should give a strong indication of the quality and true composition of the glasses. The second objective of this thesis is to confirm that the first crystallization product for all compositions is the *fcc* $NiTi_2$-type structure. Both of these objectives will be prerequisites for future, detailed studies on the electronic properties of the amorphous and crystalline states of the alloy system. In the following chapter, details of the fabrication and characterization of the $Fe_xCo_{1-x}Zr_2$ samples as well as the methodology used for the resistivity measurementsare described. In Chapter 3, the results of the various sample characterization techniques are discussed and an analysis of the resistivity measurements is presented. A summary of the experimental results and conclusions along with suggestions for future work are provided in Chapter 4.

Chapter 2

Experimental Methods

For a proper study of metallic glasses, "good", "clean" samples are required. What is meant by "good" and "clean"? It is important for the measured sample composition to be as close as possible (within ~1 at.%) to the nominal composition. The amorphous ribbons should be free of crystallites. The crystalline counterparts should be single-phased cubic with no oxides present. Hence, in this chapter, details of the sample preparation and characterization along with the methodology of the resistance measurements are given.

2.1 Preparation of the Samples

2.1.1 Ingot Preparation

The raw materials used in the preparation of the $Fe_xCo_{1-x}Zr_2$ (with $0 \leq x \leq 1$) alloys are listed below:

- Iron (Fe)
    - Aldrich Chemical Company Inc.
    - Milwaukee, Wisconsin 53233 USA
    - Morphology: chips
    - Purity: 99.9+%
- Cobalt (Co)
    - Atlantic Equipment Engineers
    - Bergenfield, New Jersey 087621 USA
    - Morphology: 1/4 - 1 inch pieces
    - Purity: 99.9%
- Zirconium (Zr)
    - Teledyne Wah Chang Albany
    - Albany, Oregon 97321-0136 USA
    - Morphology: crystal bar
    - Purity: 99.95%

Small pieces (~1 gram) of the raw elements were first etched to remove any surface contaminants. The pieces of cobalt were etched in a solution of $HCl + H_2O_2$ (3:1) and those of zirconium in $H_2O + HF + H_2O_2$ (20:1:1). Once a silver appearance to the surface was obtained, the pieces were removed from the etchant and immersed in distilled water to stop any further reaction. The metals were then rinsed with ethanol to accelerate the drying process.

Appropriate amounts (i.e., within 0.005 wt.% of the correct stoichiometry) of the constituent elements – Fe, Co, Zr – were arc-melted under zirconium-gettered prepurified (99.998%) argon gas to form ingots of approximately 4 grams in mass. These ingots were remelted 2-3 times, under the same conditions, to ensure their homogeneity.

2.1.2 Amorphous Ribbon Production

The amorphous $\mathrm{Fe}_x\mathrm{Co}_{1-x}\mathrm{Zr}_2$ alloys studied in this thesis were prepared using the melt-spinning technique. A brief overview of the technique is given below along with an account of the experimental procedure followed here.

Rapid Solidification – Melt-Spinning

Metallic glass formation requires the rapid solidification of the molten form of the material. The melt-quenching process is characterized by the continuous increase in viscosity of the melt. By comparison, crystallization of the melt occurs as a discontinuous solidification at the liquid-solid interface [4,14]. The metastability of the amorphous state and the thermodynamic stability of the crystalline state ensure that the formation of the amorphous phase will be suppressed if crystal growth is given the chance to take place. Therefore, glass formation demands that cooling be sufficiently fast to prevent the nucleation and growth of crystallites.

The melt-spinning technique yields the high cooling rates (i.e., $10^6 - 10^7$ K/s) needed to produce a metallic glass [14,15]. It involves a jet of liquid metal impinging on a rapidly rotating heat-sink where the jet is reshaped and solidified. Upon solidification, the glassy ribbon is expelled from the surface of the wheel. Some of the parameters [1] which are important in the melt-spinning method of quenching the melt are discussed below.

Wheels:

The primary goal is to select a wheel material which will transport heat swiftly and continuously away from the ribbon. Because of its excellent conducting properties, copper is the material most commonly used. The surface finish and cleanliness of the wheel greatly influence the quality and form of the cast ribbon. Continuous use of the wheel creates a problem of surface wear. However, this problem may be circumvented by refinishing the wheel following each use.

Wheel Speed:

The wheel speed controls the quenching rate and as such is the single most important parameter in the melt-spinning technique. For the most part, increasing the rotation speed of the wheel decreases the thickness of the ribbon. A rotation speed of 50 m/s produces a ribbon which is ~ 20 μm thick and $\sim$2 mm wide.

Chamber Atmosphere:

Dependent on the physical and chemical properties of the alloy, melt-spinning may be carried out in vacuum or in an atmosphere of air, inert gas, or reactive gas. Alloys susceptible to oxidation are cast in vacuum or in an inert gas atmosphere. Chamber atmosphere affects the smoothness of the surface and edges of the ribbon. Alloys cast in helium may have smooth, even edges and wheel-side surfaces which mirror the wheel surface. The same alloys cast in argon may have jagged edges and wheel-side surfaces exhibiting indentations [1].

Ejection Presssure:

Gas pressurization is used to eject the molten alloy from the crucible. Generally, an inert gas is used. Ejection pressures (typical gauge pressures between 5 and 70 kPa [1]) are dependent on the desired melt delivery rate. High ejection pressures improve the wetting pattern and, consequently, the thermal contact of the melt with the wheel.

Experimental Details

The amorphous ribbons of the $Fe_xCo_{1-x}Zr_2$ alloys were prepared using the single-roller melt-spinning technique shown in Fig. 2.1.

A small (~1 g) piece of alloy was placed in a quartz tube which had a narrow (~0.45 mm) orifice at one end. This quartz crucible was placed inside a sealed chamber and positioned over a polished copper wheel – which was refinished with fine sandpaper and cleaned with alcohol following each use. The entire chamber was then evacuated to 1.3×10^{-3} kPa and backfilled with 99.995% pure helium gas (~17

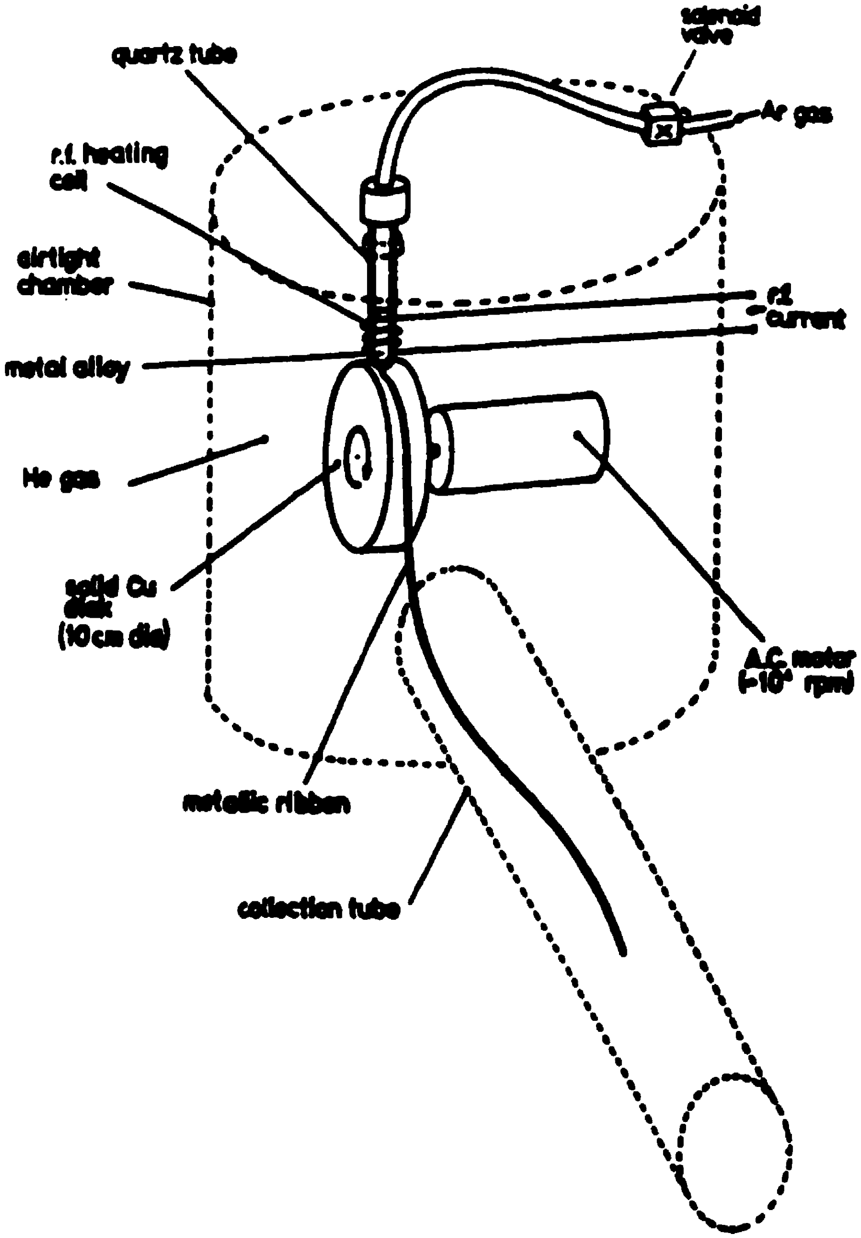

Figure 2.1: A schematic diagram of the melt-spinning apparatus. Taken from [16].

kPa) to avoid oxidation and improve the quench. An ac motor was used to provide a tangential wheel speed of ~50 m/s (wheel diameter = 10 cm, frequency $\approx 10^4$ rpm). A water-cooled, radio frequency induction coil, powered by a LEPEL High Frequency RF-generator, was used to melt the alloy button. The molten material was forced through the tube orifice and onto the rotating copper wheel by applying (by means of a manually operated solenoid valve) an argon gas pressure of ~100 kPa to the top of the tube. The alloy, in contact with the wheel, cooled and solidified extremely fast. A decrease in temperature of about 1000 K occured in about a millisecond i.e., a cooling rate of approximately 10^6 K/s was achieved. A solid ribbon of metallic glass was spun off the wheel and deposited inside a collection tube.

The melt-spinning parameters (i.e., wheel speed, tube-orifice diameter, orifice-wheel distance and melt temperature) were monitored so as to make certain that all of the $Fe_xCo_{1-x}Zr_2$ ribbons were manufactured under the same conditions. The resulting ribbons were typically 0.5-1 mm wide and about 20 μm thick.

2.1.3 Crystallization of the Samples

Small quantities of crystalline $Fe_xCo_{1-x}Zr_2$ alloys were needed for the subsequent study of the resistivity behaviour of this system. These samples were obtained by crystallizing their glass counterparts in a differential scanning calorimeter (DSC).

Two to three pieces of amorphous ribbon, each approximately 5 mm in length, were encapsulated in aluminum pans and placed inside the sample holder of a Perkin Elmer DSC-2c. High purity (99.995%) argon gas was flowed over the sample area to prevent oxidation. The calorimeter was then programmed to heat the ribbon sample to a temperature past the point of crystallization T_x. Several of the alloys (namely, the cobalt-rich $CoZr_2$, $Fe_{0.1}Co_{0.9}Zr_2$, and $Fe_{0.2}Co_{0.8}Zr_2$) exhibit a second crystallization in the temperature range from 300 to 800 K. Extra care was needed when heating samples of these compositions; to ensure the single-phase, cubic, nature of the crystallization products, it was necessary to heat to a point below the onset of the second crystallization. (The exact procedure adopted to obtain the crystallization temperatures is described in Section 2.2.3.)

Upon heating to the desired temperature at a rate of 40 K/min, the sample was then immediately cooled (at the maximum rate of 320 K/min) down to room temperature before being removed from the sample holder of the calorimeter. Once at room temperature, the sample was removed from the aluminum pan without fear of oxidation.

2.2 Sample Characterization

The composition and state of the ternary compounds were characterized by means of X-ray diffraction, electron microprobe analysis, and differential scanning calorimetry. Brief descriptions of each of these methods are given in the following sections.

2.2.1 Electron Microprobe

The electron microprobe technique was employed to verify the chemical composition and homogeneity of the metallic glasses.

This commonly employed method is non-destructive and suitable for small samples provided their surface is coated with a thin, conducting, transparent film [2]. In this case, the ribbon sample was placed onto double-sided tape, mounted on a glass slide, and electrically grounded by applying a thin film of carbon. The mounted sample was then bombarded with electrons of energy 15 keV in order to excite inner electrons to higher energy levels. The excitations quickly decayed to the ground state emitting characteristic X-ray radiation. The wavelength and intensity of the outgoing radiation was used to identify the type and concentration of emitting, constituent atoms. The analysis was done at different positions along the sample to check its compositional homogeneity. However, the apparatus employed was quite complex and several corrections had to be made before obtaining the final atomic concentrations. The accuracy of the instrument allows the concentrations of most elements to be determined to within 0.2 at.%.

2.2.2 X-ray Diffraction

The structural state of the intermetallic alloys studied here was examined by way of conventional X-ray scattering using an automated Nicolet-Stöe powder diffractometer in reflection mode. A sketch of the geometry of such an experiment is shown in Fig. 2.2.

The source beam consisted of $\mathrm{Cu}K_\alpha$ ($\lambda = 1.5418$ Å) radiation, selected so that the wavelength $\lambda = hc/E$ of the incident photons was comparable to the interatomic spacings and the first peak of the amorphous diffraction pattern spanned a scattering angular range of $2\theta \sim 25^\circ - 50^\circ$. The incident beam was focussed using Soller slits set 2 mm wide. The diffracted beam was passed through a graphite monochromator to remove most of the contributions from incoherent scattering such as fluorescence and air scattering. As such, mainly the coherent scattering from the sample was allowed to enter the scintillation detector. The measured quantity was the scattering interference function $I(\mathbf{q})$, where the magnitude of the scattering vector $\mathbf{q}$ is related to the angle 2θ between outgoing X-ray ($\mathbf{K_{out}}$) and incoming X-ray ($\mathbf{K_{in}}$), see

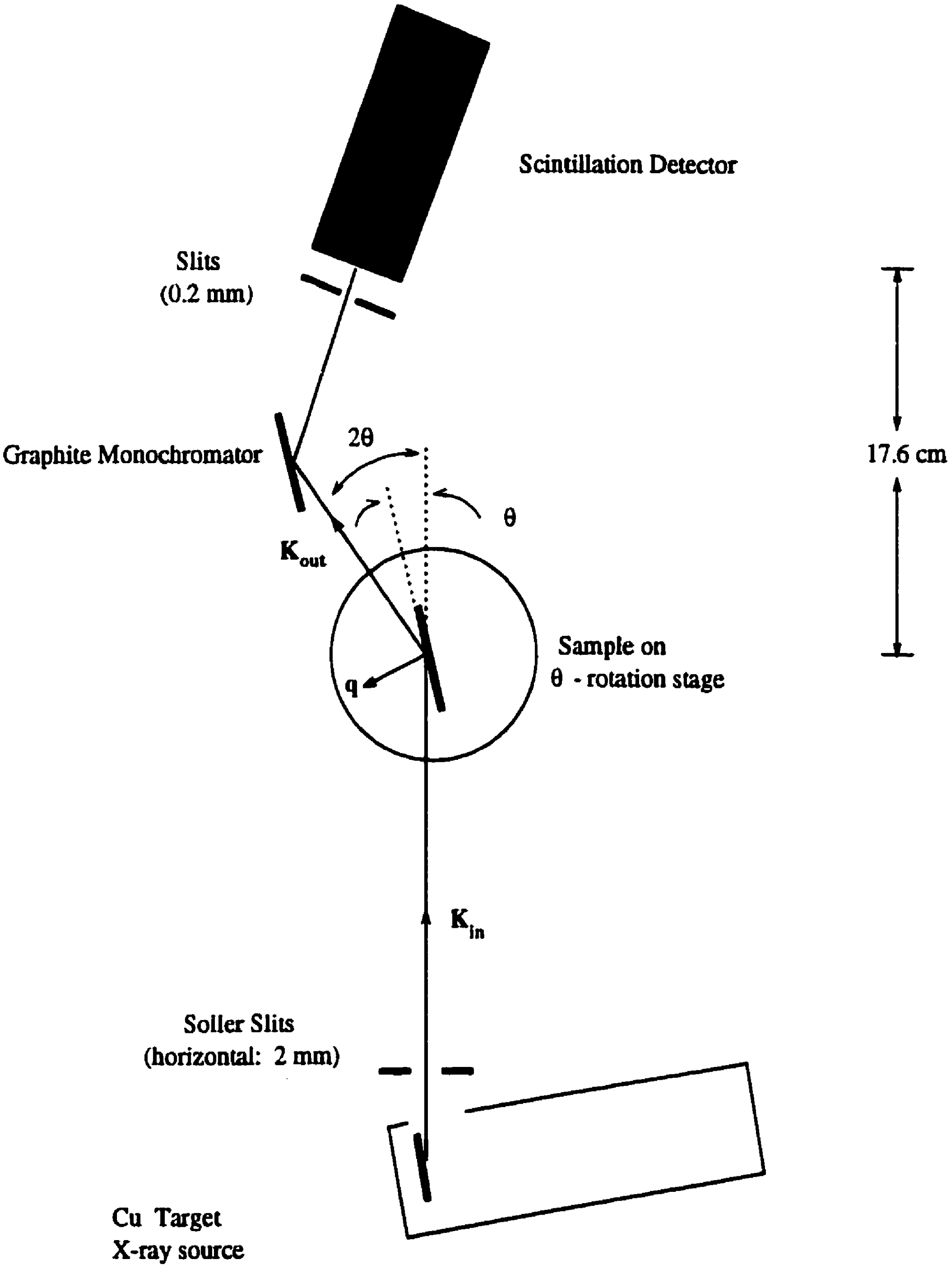

Figure 2.2: A schematic view of the X-ray diffractometer.

Fig. 2.2, by

$$\mathbf{q} = \mathbf{K}_{\mathbf{out}} - \mathbf{K}_{\mathbf{in}} = \frac{4\pi\ sin\theta}{\lambda} \tag{2.1}$$

For use with this particular diffractometer, short strips of the amorphous (or crystalline, as the case may have been) alloy were stuck onto double-sided tape mounted on a glass slide. The dimensions of a single strip were typically 10 × 0.5 × 0.02 mm^3. The total area covered by the sample was ~1.2 cm^2, which was sufficient to achieve precise and accurate results. Most of the X-ray scans for the amorphous (crystalline) samples were performed in the 2θ range from 25° to 80° (25° - 55°) at incremental steps of 0.1° (0.1°), and a counting time of 10 seconds (30 seconds) at each position.

2.2.3 Differential Scanning Calorimetry

Heat is either absorbed or liberated whenever a material undergoes a chemical reaction or a change in physical state such as melting or transition from one crystalline state to another. Many of these processes can be activated simply by raising the temperature of the material. Differential scanning calorimeters are employed to determine the enthalpies and temperatures of such transitions [17]. This is accomplished by measuring the heat flow needed to maintain a sample of the material and an inert reference at the same temperature.

For the purpose of this work, a Perkin Elmer Differential Scanning Calorimeter DSC-2c, (shown schematically in Fig. 2.3) was used to determine the crystallization temperatures and enthalpies of the $Fe_xCo_{1-x}Zr_2$ alloys. Approximately 5 mg of sample were sealed in an aluminum pan and placed into the sample holder (one of two resistively-heated holders whose individual temperatures were monitored by two separate resistance thermometers). Dry, high purity argon was flowed through

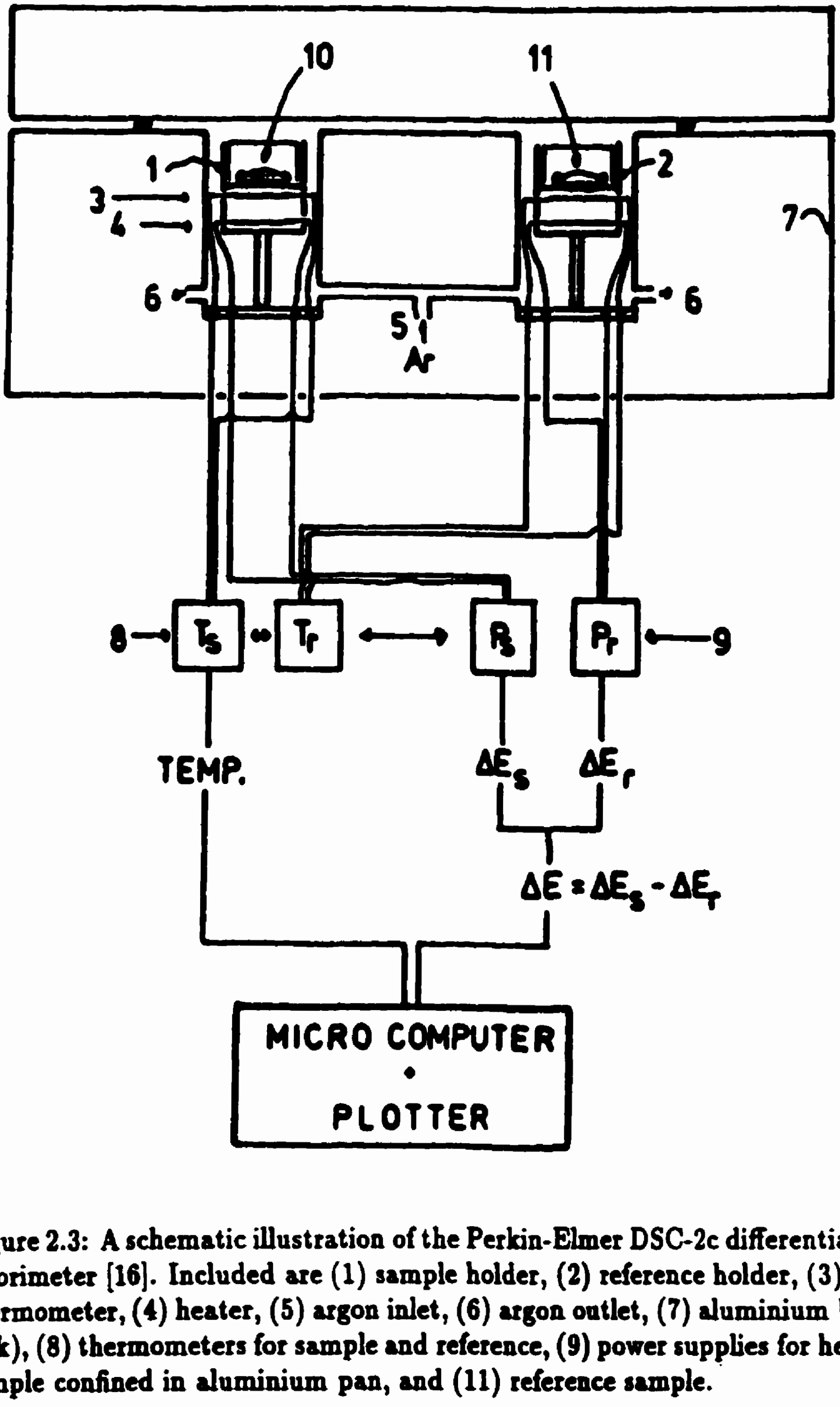

Figure 2.3: A schematic illustration of the Perkin-Elmer DSC-2c differential scanning calorimeter [16]. Included are (1) sample holder, (2) reference holder, (3) resistance thermometer, (4) heater, (5) argon inlet, (6) argon outlet, (7) aluminium body (heat sink), (8) thermometers for sample and reference, (9) power supplies for heaters, (10) sample confined in aluminium pan, and (11) reference sample.

the sample area to prevent oxidation. The two holders were then programmed to be heated linearly at a rate of 40 K/min to 800 K. The difference in the electric power needed to maintain the two holders at the same temperature was recorded as a function of temperature. Once the final temperature was reached, the sample was immediately cooled (at the maximum rate of 320 K/min) to prevent oxidation. Since the crystallization process of interest here is irreversible, a second scan of the sample was made immediately following the first. The resulting scan was then subtracted from the initial one thereby reducing the effects of any instrumental drifts or background noise.

2.3 Density Measurements

The measurement of the density is important for a systematic examination of the electronic properties of metallic glasses with those of their crystalline counterparts. Any such comparison can be misleading unless materials of approximately equivalent densities are considered.

For melt-spun amorphous samples, the measurement of density does not present a problem. The densities of the $Fe_xCo_{1-x}Zr_2$ ribbons were measured by applying Archimedes' principle: *A body immersed in a liquid displaces a volume of liquid equal to its own.* The density in air of this body can be determined by measuring its weight in air, W_{air}, and its weight in a liquid medium, W_{liquid}. Next, applying the principle,

$$\frac{m_{sample}}{d_{sample}} = V_{sample} = V_{liquid} = \frac{m_{liquid}}{d_{liquid}} \tag{2.2}$$

With the mass of the displaced liquid determined by

$$\Delta\, m = \frac{W_{air} - W_{liquid}}{g} \tag{2.3}$$

the density of the sample is

$$\begin{aligned} d_{sample} &= d_{liquid}\frac{m_{sample}}{m_{liquid}} \\ &= d_{liquid}\frac{m_{sample}}{\Delta\, m} \\ &= d_{liquid}\frac{W_{air}}{W_{air} - W_{liquid}} \end{aligned} \tag{2.4}$$

In the case of this work, a Mettler H20T mechanical balance was used for the weighing. Two measuring platforms each consisting of metal wire wound into the form of a spiral and connected together by an amorphous metal fiber (~15 μm in diameter) were suspended from the balance arm in such a way as to have the lower platform immersed in the liquid.

The sample dimensions were, on average, $25 \times 0.5 \times 0.02$ mm^3 and the mass typically totalled 15 mg. Liquid tetrabromoethane ($C_2H_2Br_4$ density = 2.97 g/cm^3) was selected for the medium because of its high density and low surface tension. To further improve the accuracy of the results, the samples were measured several times to reduce the systematic errors due to temperature and air draft perturbations.

2.4 Resistance Measurements

2.4.1 Room Temperature Resistance of a-$Fe_xCo_{1-x}Zr_2$

The room-temperature electrical resistance of the metallic glasses was measured using a 4-probe dc technique. A schematic diagram of the experimental set-up is provided in Fig. 2.4.

A ribbon of amorphous alloy of approximately 50 cm in length was clamped at the ends to a rectangular piece of plexiglass. A pair of copper, pressure-point contacts were placed at each end of the sample.The outermost pair served as current leads while the innermost pair was used to measure the potential drop across the

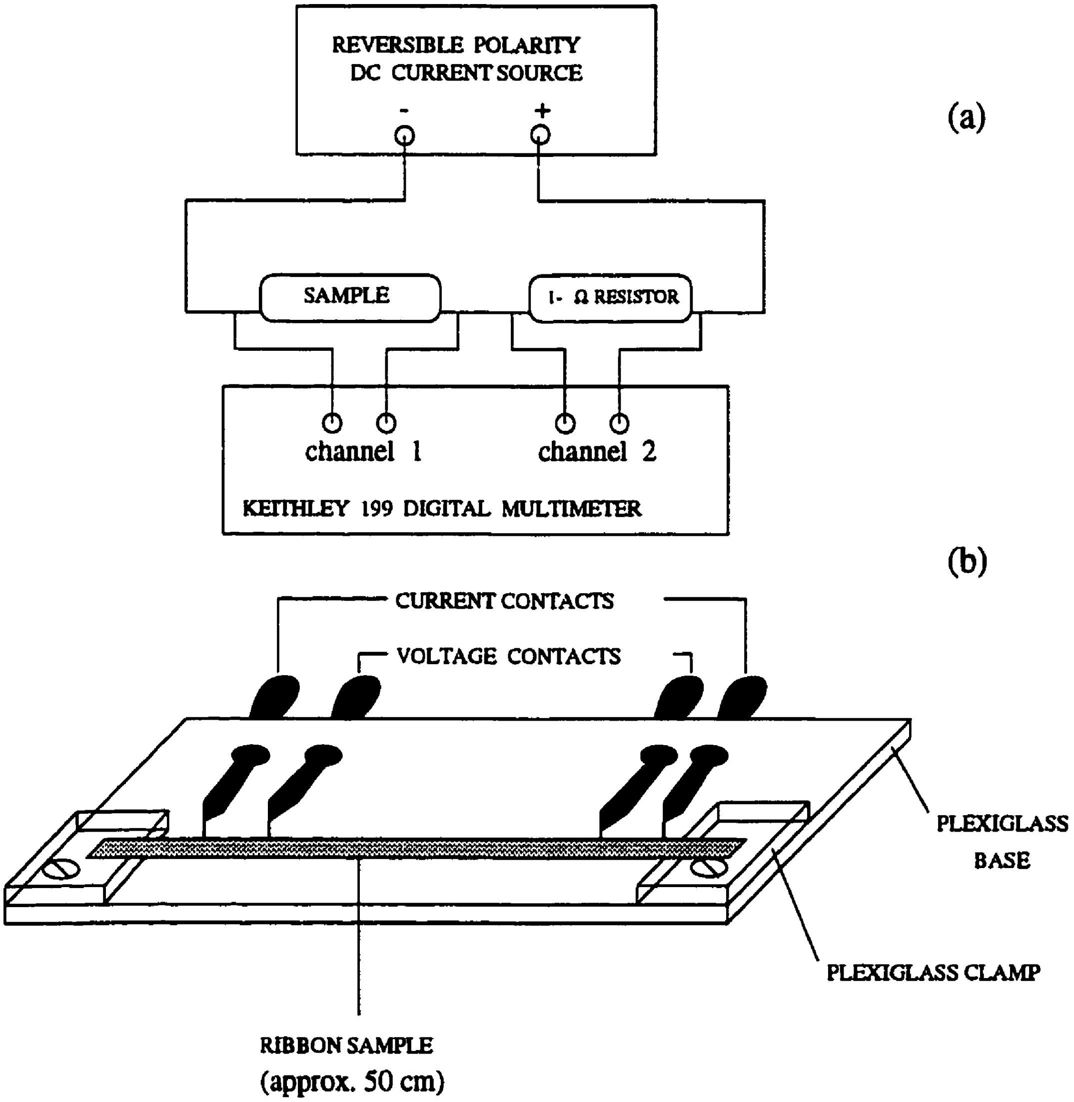

Figure 2.4: (a) A schematic representation of the experimental set-up employed for measuring the room-temperature resistance of the ribbons. (b) A detailed view of the sample holder.

ribbon. Current (~50 mA) was supplied by a Keithley 225 dc current source. The voltage was measured using a multi-channel Keithley 199 Digital Multi-Meter.

For an accurate determination of the resistance of the sample, it is necessary to know the actual amount of current being supplied as well as the true voltage drop. By measuring the potential difference across the 1-Ω standard resistor (see Fig. 2.4), it was possible to calculate the current using Ohm's law: $R_{1\Omega} = V_{1\Omega} \,/\, I$. Obtaining the voltage, on the other hand, was less straightforward because of the contact potential which may exist at the junction between sample and contact. Furthermore, if a temperature difference exists between contacts, an emf known as the Seebeck (or thermoelectric) emf [3] will be generated. To remove their contribution to the total voltage measured, a second measurement with the polarity of the current reversed was taken. Because the Seebeck emf and contact potential do not depend on the current, subtracting the second measured value from the first effectively cancelled their contribution to the voltage leaving only the potential across the sample due to the current, V_{drop}:

$$V_{+}{}^{tot} = V_{drop} + V_{Seebeck} + V_{contact} \tag{2.5}$$

$$V_{-}{}^{tot} = -V_{drop} + V_{Seebeck} + V_{contact} \tag{2.6}$$

and

$$V_{drop} = \frac{1}{2}\left(V_{+}{}^{tot} - V_{-}{}^{tot}\right) \tag{2.7}$$

where $V_{+}{}^{tot}$ was the total voltage measured when a current I was passed through the sample, and $V_{-}{}^{tot}$ was the total voltage measured when a current $-I$ was applied. With the true values of the current and voltage, the room-temperature resistance of the ribbon sample was calculated using, once again, Ohm's law.

2.4.2 Temperature-Dependent Resistance Measurements

Changes in resistance with temperature for both the metallic glasses and their crystalline counterparts were examined using a four-terminal ac bridge technique.

Some preparation with regards to the alloy samples was needed before any measurements could be taken. Voltage and current leads, consisting of 45-gauge (stripped) copper wire, were fixed onto a strip of sample roughly 0.5 cm in length with a small amount of conductive silver epoxy [18]. In order to reduce contact resistance and accelerate the curing process of the epoxy, the sample-lead assembly was annealed at 110 °C for approximately two hours. The sample was then mounted onto one side of a mylar-coated piece of copper (12 × 16 × 0.5 mm^3) using some GE varnish. The thin film of mylar served as an electrical insulator between the metallic sample and copper base.

For the next stage, the sample mount was secured with some more of the GE varnish onto the copper-block end of the resistance probe and appropriate electrical connections were made between the sample and copper leads housed within the four thin-walled stainless steel rods of the probe. A diagram of the resistance probe assembly is provided in Fig. 2.5. A calibrated platinum resistance thermometer (Lake Shore Cryotronics Model Pt-111) located at the tip of the probe was employed to monitor the temperature of the sample. The accuracy of the thermometer varied from 20 mK at 80 K to 0.1 K at 300 K. An excitation voltage of 2 mV was applied across the sample. Changes in the resistance and temperature of the sample were detected using an ac bridge in conjunction with an eight-sensor multiplexor (Linear Research Inc. Models LR-700 and LR-720-8, respectively). A sensitivity of 10^{-5} Ω was easily achieved with this device and was more than adequate for the 10 mΩ overall changes measured here.

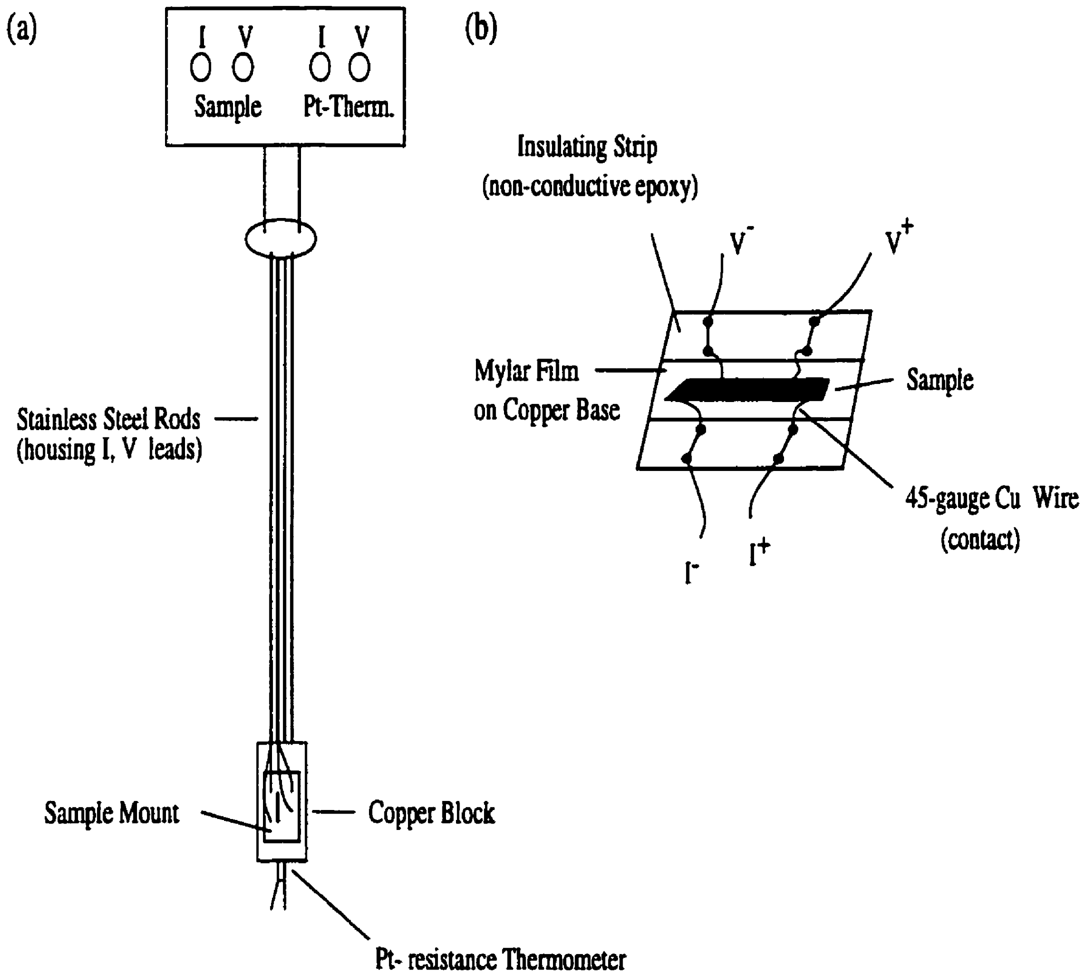

Figure 2.5: Schematic diagrams of (a) the probe-assembly used in the determination of the temperature-dependence of the resistance, and (b) the sample mount.

The effect of temperature on the resistance of the alloys was examined in the range between 80 K and 300 K. This was accomplished with the experimental arrangement, using a nitrogen-based cryostat, presented schematically in Fig. 2.6. With the probe encased in the series of concentric quartz tubes which make up the cryostat, the sample chamber was then evacuated to $\sim$1 kPa. The temperature within the chamber was then decreased by introducing liquid nitrogen into the coolant chamber. To obtain a controlled and sufficiently slow cooling rate, the space between the sample and coolant chambers was diffusion-pumped to 1.3×10^{-9} kPa. Once the temperature had dropped to near 200 K, 69 kPa of helium gas was introduced into the chamber containing the sample to facilitate further cooling down to 80 K – the helium gas providing a medium for transferring the "cold" to the sample. The values of the resistance and temperature of the sample were recorded every six seconds. The data was collected using the LABVIEW software which accompanied the LR-700 ac bridge and a Macintosh IIci personal computer.

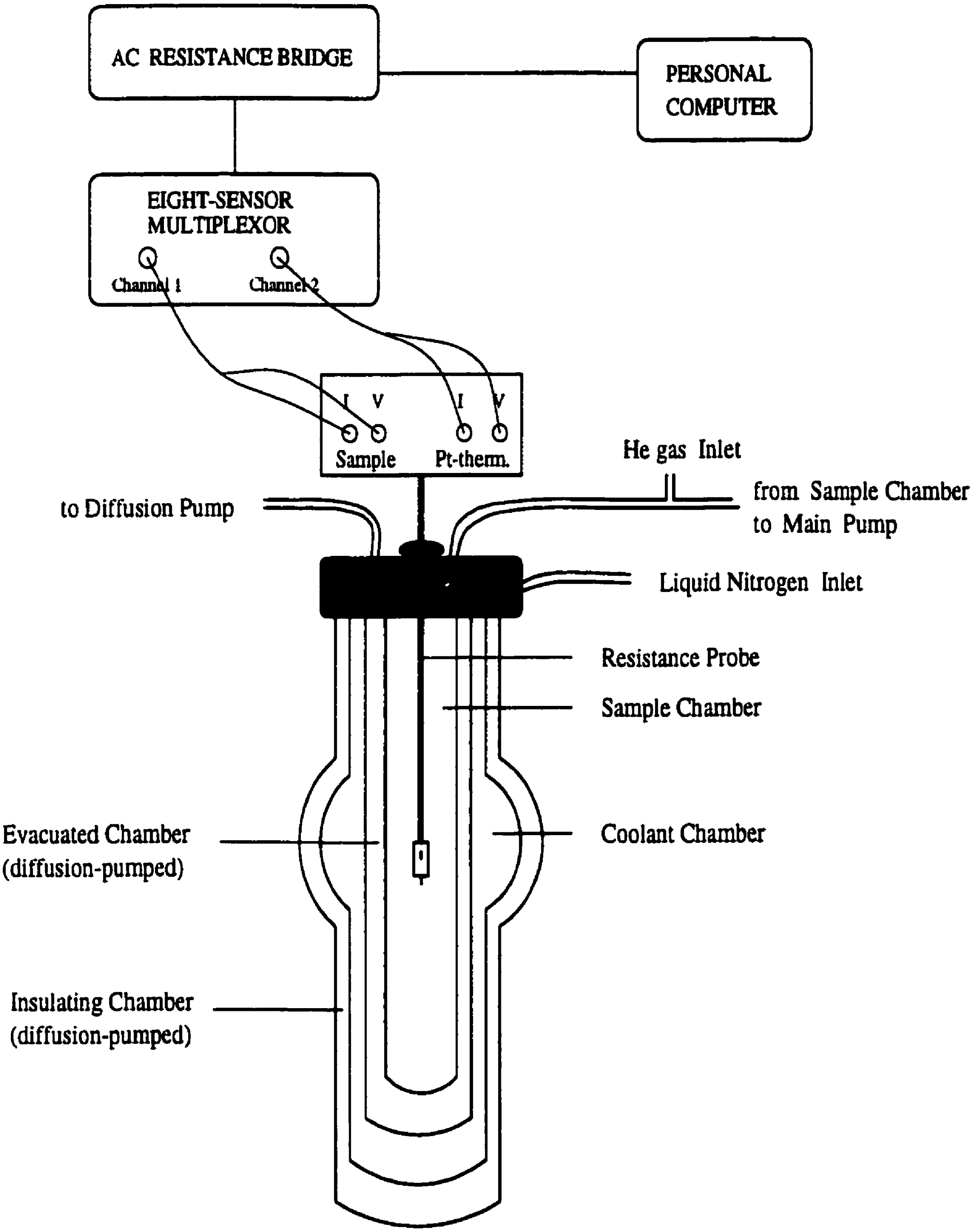

Figure 2.6: Schematic arrangement of the nitrogen-based cryostat used to measure changes in the resistance of the samples over the temperature range of 80 to 300 K.

Chapter 3

Results and Discussion

3.1 Sample Characterization

3.1.1 Chemical Composition of the a-$[\mathrm{Fe}_x\mathrm{Co}_{1-x}]_{33.3}\mathrm{Zr}_{66.7}$ Alloys

The elemental composition and homogeneity of the a-$[\mathrm{Fe}_x\mathrm{Co}_{1-x}]_{33.3}\mathrm{Zr}_{66.7}$ ribbons were established by electron microprobe analysis.

The concentrations of iron, cobalt, and zirconium were examined at several positions along each ribbon. The values of these concentrations were consistent (to within 0.3%) over the whole length of the ribbon, thus confirming its chemical homogeneity. Figure 3.1 shows the microprobe-determined concentrations of iron and cobalt for the Fe-Co-Zr ribbons plotted against the nominal concentration of iron. A slight discrepancy can be seen at the nominal Fe-concentration of 20 at.%. There appears to be less iron and even less cobalt than expected in this a-$[\mathrm{Fe}_{0.6}\mathrm{Co}_{0.4}]_{33.3}\mathrm{Zr}_{66.7}$ sample. Furthermore, Fig. 3.2 shows that the amount of zirconium contained in this sample was roughly 3% more than that anticipated. The source of this inconsistency is probably in the initial ingot-preparation stage. A slightly greater-than-intended starting mass of zirconium seems to have been the culprit. In Table 3.1, the nominal and experimentally measured compositions of all the ternary Fe-Co-

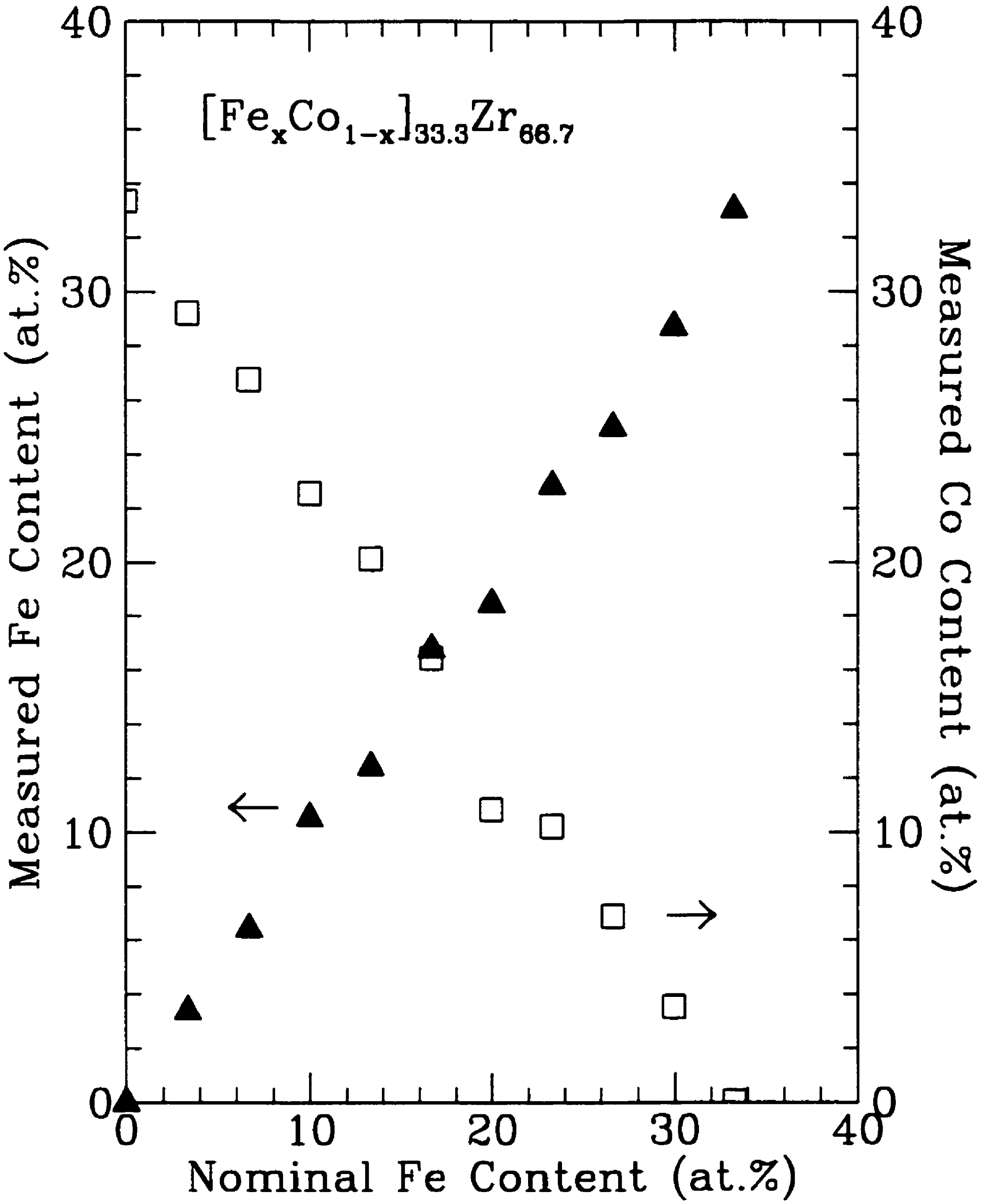

Figure 3.1: Electron microprobe determination of the concentrations of iron and cobalt for the a-$(Fe_xCo_{1-x})_{33.3}Zr_{66.7}$ ribbons.

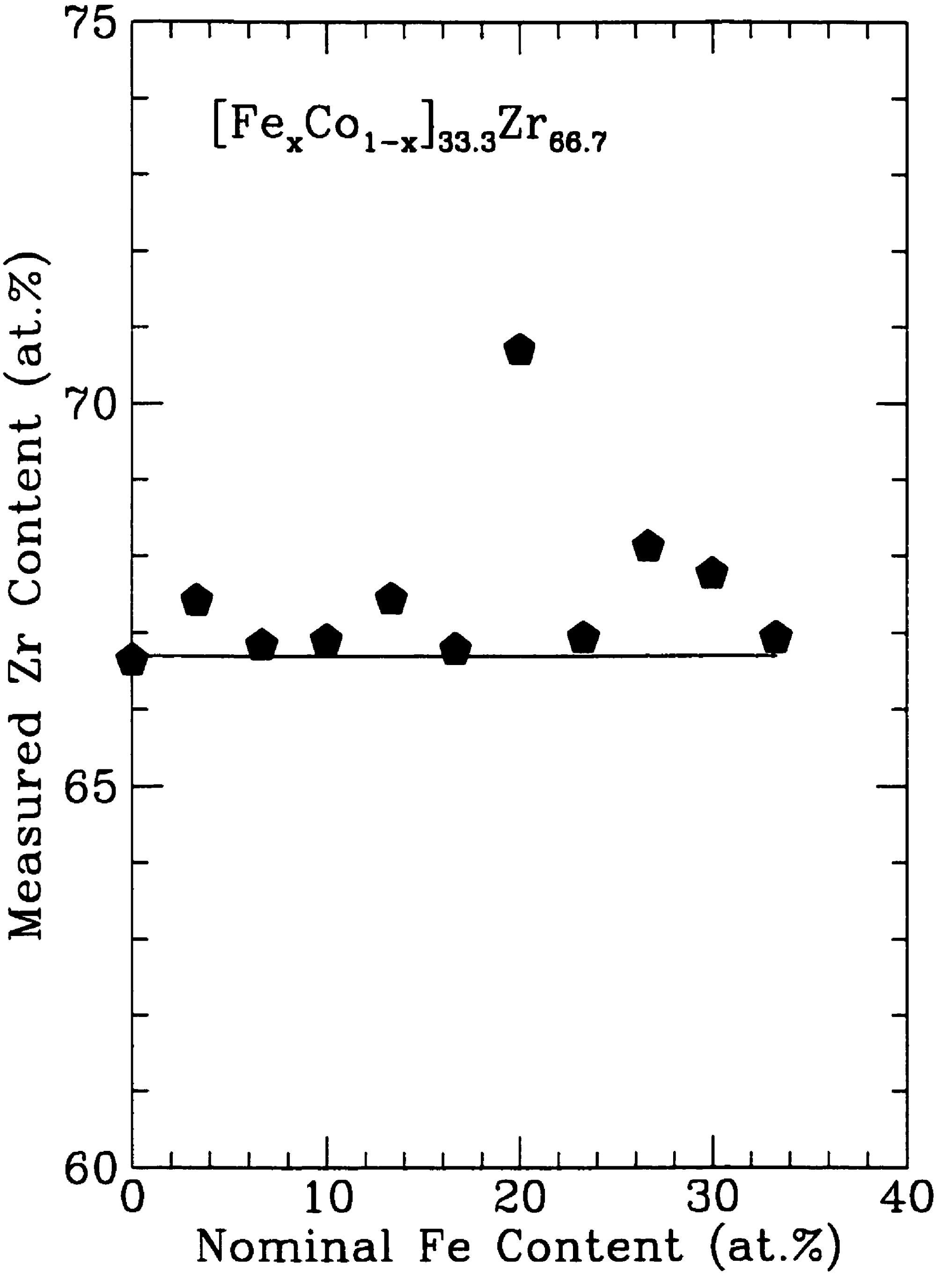

Figure 3.2: Electron microprobe determination of the concentrations of zirconium for the a-$(Fe_xCo_{1-x})_{33.3}Zr_{66.7}$ ribbons. The solid horizontal line indicates the desired nominal concentration of zirconium. The accuracy of the measurements is quoted at 0.5 at.%.

a-[Fe_xCo_{1-x}]$_{33.3}Zr_{66.7}$						
Nominal Concentrations				Analyzed Concentrations		
x	Fe	Co	Zr	Fe	Co	Zr
0	0.0	33.3	66.7	0.0	33.4	66.7
0.1	3.3	30.0	66.7	3.4	29.2	67.4
0.2	6.7	26.6	66.7	6.4	26.8	66.8
0.3	10.0	23.3	66.7	10.5	22.6	66.9
0.4	13.3	20.0	66.7	12.4	20.1	67.4
0.5	16.65	16.65	66.7	16.8	16.4	66.8
0.6	20.0	13.3	66.7	18.4	10.8	70.7
0.7	23.3	10.0	66.7	22.8	10.2	66.9
0.8	26.6	6.7	66.7	25.0	6.9	68.1
0.9	30.0	3.3	66.7	28.7	3.6	67.8
1.0	33.3	0.0	66.7	33.1	0.0	66.9

Table 3.1: Nominal and electron-microprobe-determined values of the elemental concentrations for the a-$Fe_xCo_{1-x}Zr_2$ ribbons. The accuracy of the measurements is quoted at 0.5 at.% for the elements investigated.

Zr glasses studied are listed. The concentration of each constituent element differs from the expected nominal value by less than 1 at.% – the exceptions being a-($Fe_{0.6}Co_{0.4}$)$_{33.3}Zr_{66.7}$, and to a somewhat lesser degree, a-($Fe_{0.8}Co_{0.2}$)$_{33.3}Zr_{66.7}$. The accuracy of the experimental arrangement is quoted as 0.5 at.% for the elements investigated.

3.1.2 Alloy Structure – X-ray Diffraction

Radial Distribution Function

Unlike crystalline solids, the atomic structure of non-crystalline solids cannot be precisely nor fully specified. For perfect crystals, knowledge of the Bravais lattice and the number of atomic locations contained within the unit cell, which can easily be acquired by X-ray diffraction, is enough to determine the coordinates of all the sites. Analogously, the unit cell is absent for non-crystalline solids, and X-ray diffraction yields information which is incomplete and statistical in nature.

The information extracted from the X-ray diffraction experiments about the structure of the non-periodic lattice of atoms is in the form of the pair distribution function $g_2(\vec{r})$ [2]. In a homogeneous (isotropic) solid – as are most glasses – the distribution function depends on the separation of the atoms, i.e., r. The radial distribution function (RDF) is given by

$$G(r) = 4\pi r^2 n\ g_2(r) \tag{3.1}$$

where $ng_2(r)$ represents the number density of atoms at a distance r from a reference atom. With increasing r, $G(r)$ exhibits a parabolic behaviour and details of the structure are averaged out. To avoid the rapid increase in slope for large r, the differential RDF

$$G'(r) = 4\pi r^2 n\ [g_2(r) - 1] \tag{3.2}$$

is used (for which the large asymptote is zero) [2]. Note that this expression is related to the structure factor $S(\vec{q})$ (where q is the magnitude of the scattering vector):

$$G'(r) = \frac{2r}{\pi} \int_0^\infty q[S(q) - 1] \sin(qr) dq \tag{3.3}$$

or equivalently (by taking the Fourier transform),

$$q[S(q) - 1] = \int_0^\infty G'(r) \frac{\sin(qr)}{r} dr \tag{3.4}$$

$S(q)$ is in turn related to the experimentally-measured, elastic scattering intensity per atom [19]

$$\begin{aligned} S(q) &= \frac{I(q)}{|f(q)|^2} \\ &= 1 + n\int_0^R g_2(r)\frac{\sin(qr)}{qr}4\pi r^2 dr, \end{aligned} \tag{3.5}$$

where $|f(q)|^2$ is known as the atomic form factor and represents scattering of the radiation from an individual atom.

As already mentioned, the pair distribution function is the most information that can be obtained from diffraction experiments. Clearly, a complete description of the pair correlation in an n-component alloy amounts to measuring $n(n+1)/2$ pair distribution functions.

Structural Data

The structure of both the amorphous and crystalline $[\mathrm{Fe}_x\mathrm{Co}_{1-x}]_{33.3}\mathrm{Zr}_{66.7}$ samples was verified by graphite-monochromated CuK_α X-ray diffraction.

With the experimental set-up as shown in Fig. 2.2, a minimum crystalline fraction of 0.1% can be detected. If crystallites were to form, they would have done so preferentially on the *free* side of the ribbon i.e., that side which was not in contact with the wheel during melt-spinning and cooled much more slowly than the wheel-side surface. For this reason, the diffraction scans were done on the free side of the ribbon. Typical diffractograms for a-$[\mathrm{Fe}_x\mathrm{Co}_{1-x}]_{33.3}\mathrm{Zr}_{66.7}$ are presented in Fig. 3.3. The diffraction patterns exhibit two diffuse peaks (in this scan range) which are distinguishing features of glasses, and are devoid of sharp crystal spikes (Bragg peaks). The amorphous nature of the as-made glass samples was thereby confirmed.

Figure 3.4 displays several diffraction scans pertaining to the c-$[\mathrm{Fe}_x\mathrm{Co}_{1-x}]_{33.3}\mathrm{Zr}_{66.7}$. All of the spectra exhibit Bragg peaks characteristic of a crystalline phase. These

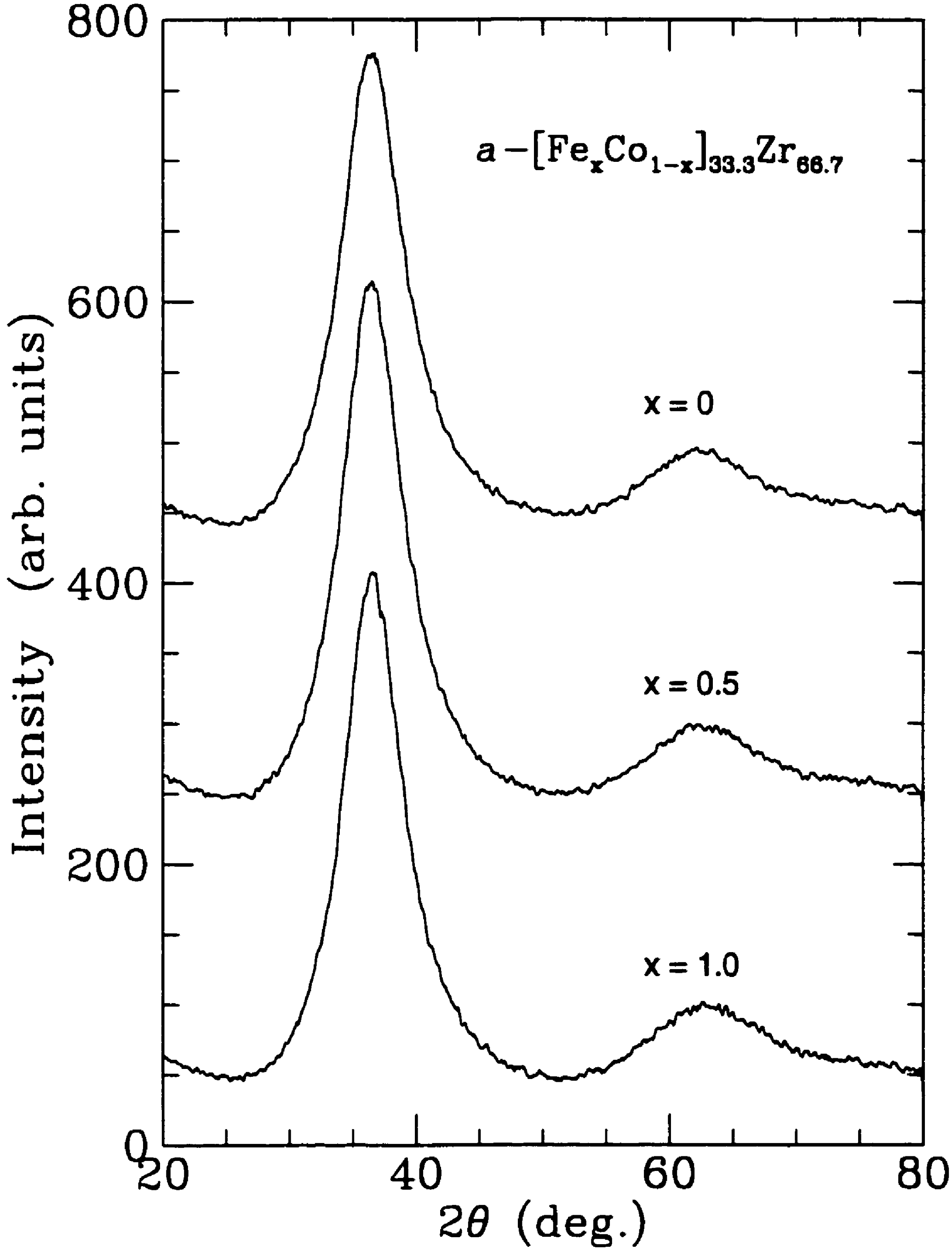

Figure 3.3: Selected X-ray diffraction patterns of a-(Fe$_x$Co$_{1-x}$)$_{33.3}$Zr$_{66.7}$ (for x = 0, 0.5, 1.0). The data have been offset for clarity.

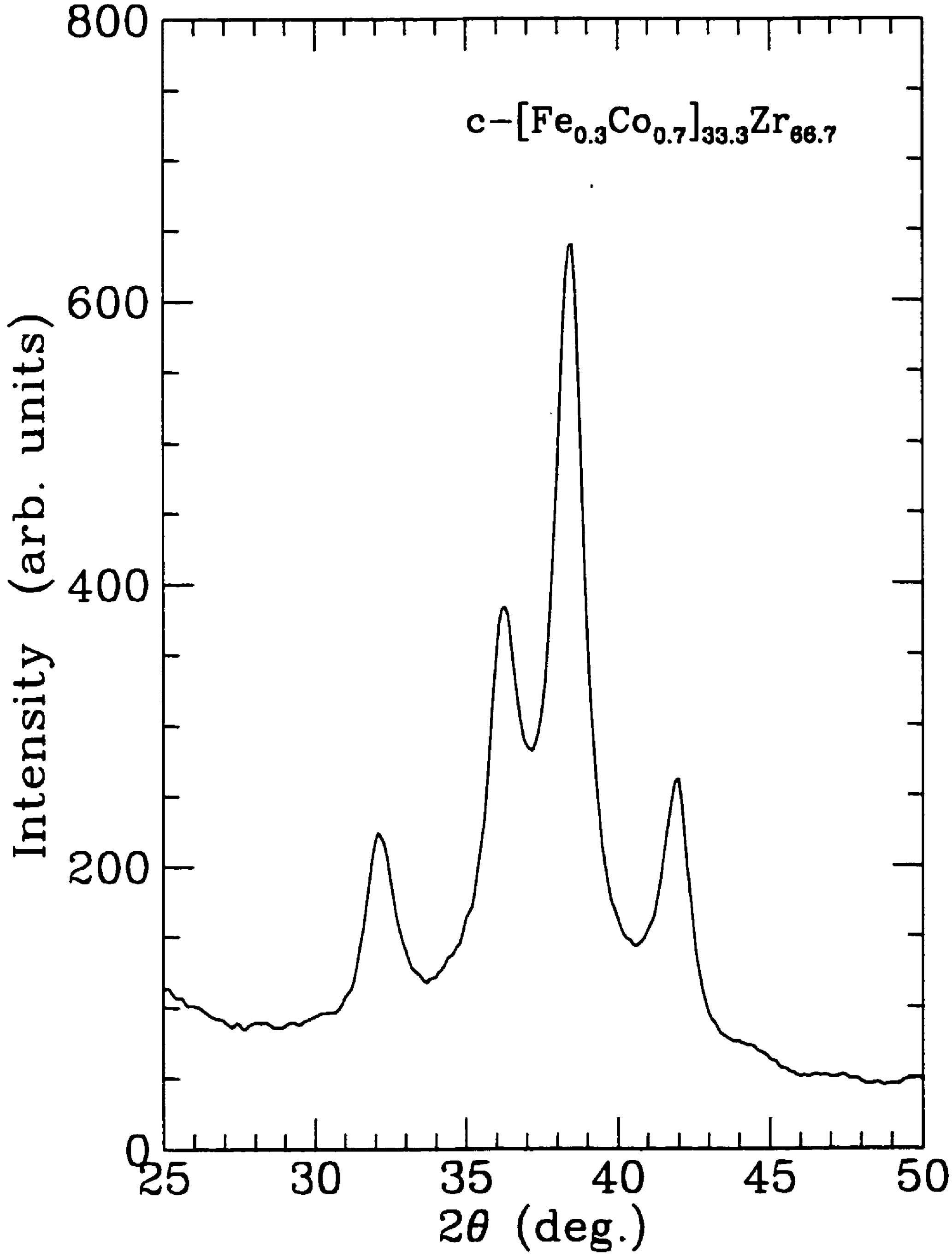

Figure 3.4: Typical X-ray diffraction patterns of crystalline $(Fe_xCo_{1-x})_{33.3}Zr_{66.7}$. The pattern shown here corresponds to the composition with $x = 0.3$.

peaks are somewhat broadened by thermal and zero-point motion. Nevertheless, they are well-defined and cannot be mistaken for the broad peaks observed for amorphous material. Furthermore, in each of the spectra, a pattern consisting of four prominent peaks (located at approximate 2θ values of $32°, 36°, 38°$ and $42°$) is evident.

In order to determine the structural phase of the crystalline compounds, three compositions – $FeZr_2$, $Fe_{0.7}Co_{0.3}Zr_2$, and $Fe_{0.5}Co_{0.5}Zr_2$ – were selected to represent the crystalline system and were then analyzed. The peak positions of each of these compositions were fitted [20] to both the $NiTi_2$-type, face-centered cubic (*fcc*) structure ($E9_3$) and the Al_2Cu-type, body-centered tetragonal (*bct*) structure ($C16$). The calculated peak positions and intensities for the *fcc* and *bct* phases are indicated in Figs. 3.5, 3.6 and 3.7. From these figures, it can be clearly seen that the samples were, for all intents and purposes, single-phased *fcc* as required. In addition, the lattice parameter corresponding to the observed peaks was determined to be, on average, 12.35 ± 0.17 which is in reasonable agreement with the reported values for $FeZr_2$ (12.14) and $CoZr_2$ (12.18) [21].

The diffraction patterns in Fig. 3.4 are typical of all the Fe-Co-Zr crystals save for crystalline $Fe_{0.6}Co_{0.4}Zr_2$. It is worth noting that the diffraction scan for the $Fe_{0.6}Co_{0.4}Zr_2$ crystal (shown in Fig. 3.8) has two additional peaks at $2\theta = 35°$ and $36.5°$, as compared with those of the other crystalline samples. Now, from the electron microprobe results discussed earlier, it is known that the Zr-concentration is $\sim$3 at.% greater for this sample. Suspecting the additional peak positions to be due to this discrepancy, the peak positions were fitted to the hexagonal close-packed (*hcp*) structure characteristic of metallic zirconium. The results of the fit confirmed this assumption.

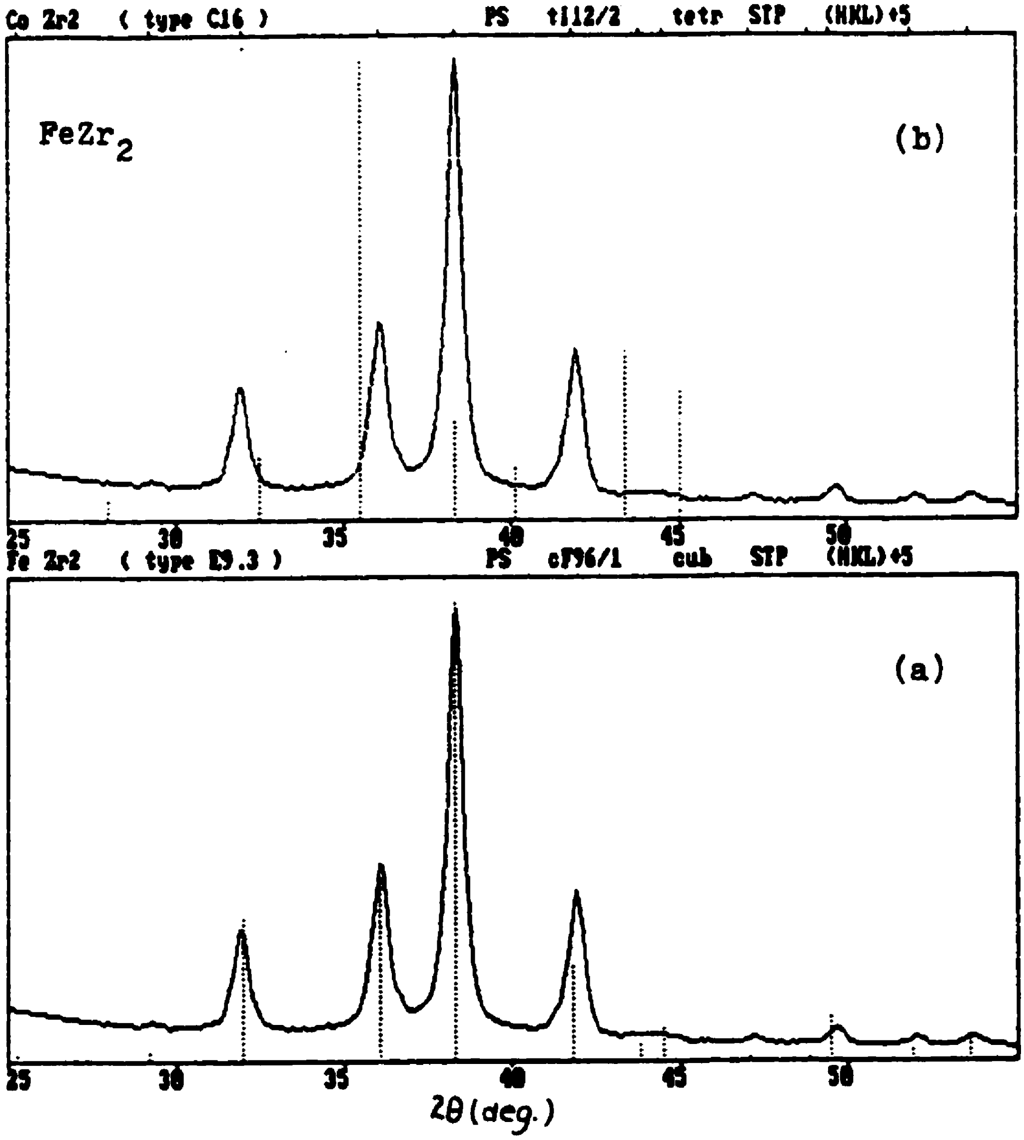

Figure 3.5: X-ray diffraction scans for crystalline $Fe_{33.3}Zr_{66.7}$. The superimposed vertical lines indicate the calculated positions and relative intensities of Bragg peaks for the (a) *fcc* and (b) *bct* structures of crystalline $FeZr_2$. The sample exhibits the *fcc* structure.

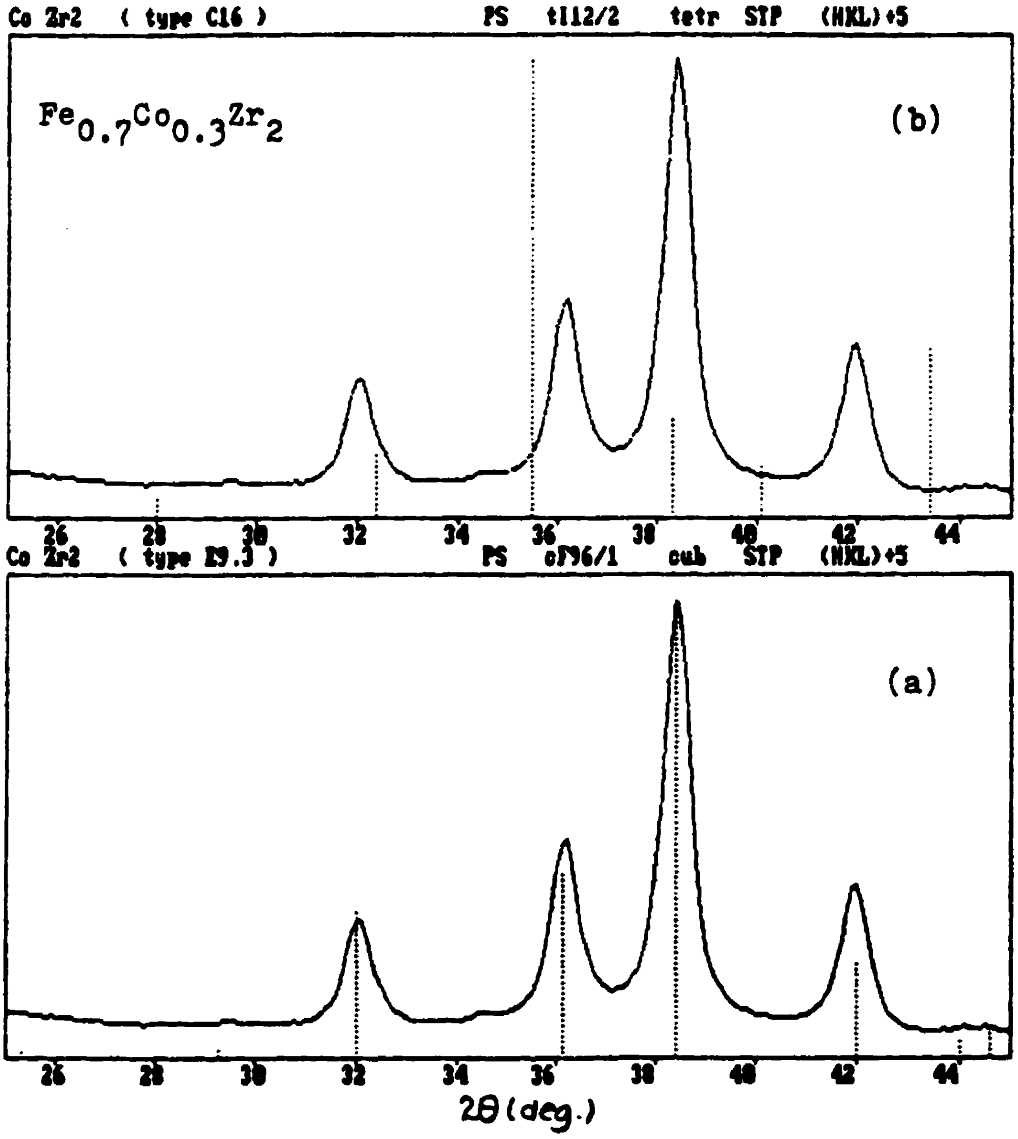

Figure 3.6: X-ray diffraction scans for crystalline $(Fe_{0.7}Co_{0.3})_{33.3}Zr_{66.7}$. The superimposed vertical lines indicate the calculated positions and relative intensities of Bragg peaks for the (a) *fcc* and (b) *bct* structures of crystalline $Fe_{0.7}Co_{0.3}Zr_2$. The sample exhibits the *fcc* structure.

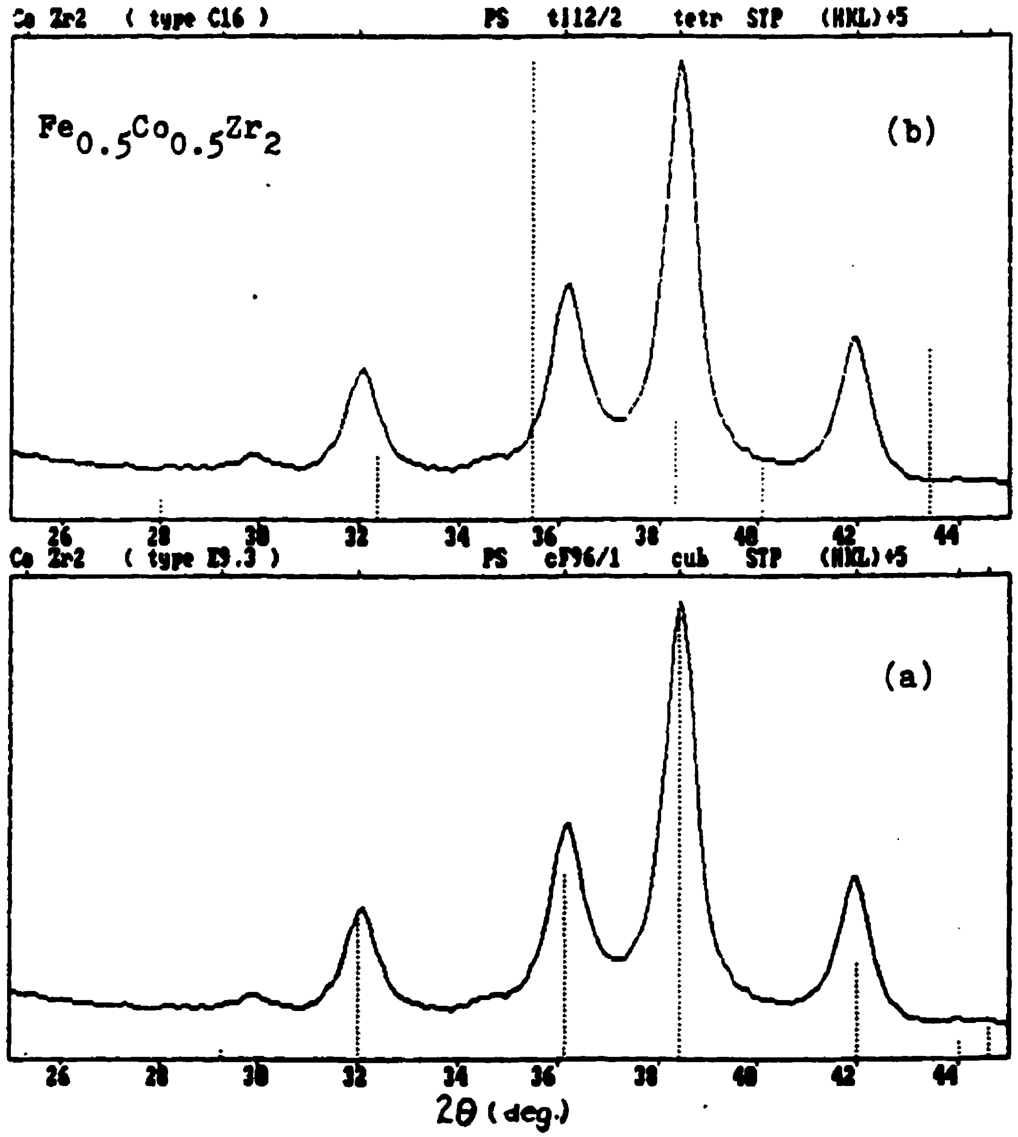

Figure 3.7: X-ray diffraction scans for crystalline $(Fe_{0.5}Co_{0.5})_{33.3}Zr_{66.7}$. The superimposed vertical lines indicate the calculated positions and relative intensities of Bragg peaks for the (a) *fcc* and (b) *bct* structures of crystalline $Fe_{0.5}Co_{0.5}Zr_2$. The sample exhibits the *fcc* structure.

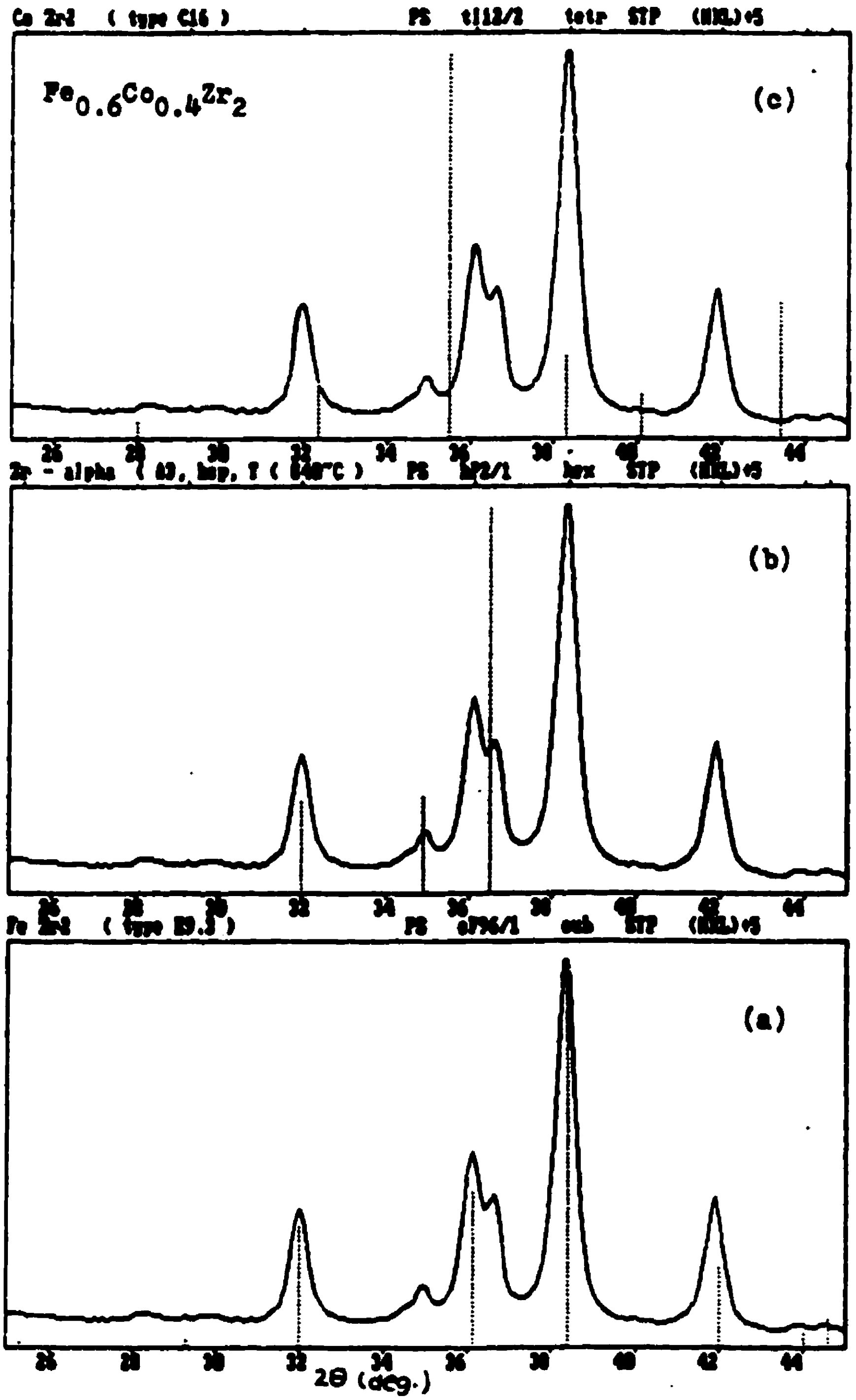

Figure 3.8: X-ray diffraction scans for crystalline $(Fe_{0.6}Co_{0.4})_{33.3}Zr_{66.7}$. The superimposed vertical lines indicate the calculated positions and relative intensities of Bragg peaks for the (a) *fcc*, (b) *hcp*, and (c) *bct* structures of crystalline $Fe_{0.6}Co_{0.4}Zr_2$. The sample exhibits both the *fcc* and *hcp* phases.

3.1.3 Temperatures and Heats of Crystallization

The crystallization behaviour of the metallic glasses provides yet another means of characterization.

The amorphous samples were heated to 800 K (at a rate of 40 K/min) in a Perkin Elmer DSC. Several of the thermograms are reproduced in Figs. 3.9 and 3.10. The temperature at which the exothermic maximum occurs is taken as the crystallization temperature, T_x and the area under the peak as the enthalpy change upon crystallization, ΔH_c. The thermograms of the cobalt-rich compositions (see Fig. 3.10) exhibit a second exothermic peak around 750 K. This second peak corresponds to a crystal-crystal transition, namely the transition from the metastable *fcc* state to that of the *bct*. The T_x corresponding to the first crystallization (to the *fcc* structure) is shown for all the ribbons in Fig. 3.11. The incongruous value for $[Fe_{0.6}Co_{0.4}]_{33.3}Zr_{66.7}$ is consistent with the earlier results of both the electron microprobe analysis and the X-ray diffraction experiments. It has been observed that the stability of a glass or its glass-forming ability increases with the atomic size difference of its constituent elements [22]. As Co is slightly smaller than Fe, this may explain the small increase in T_x (i.e., stability) as the amount of Co is increased in the $[Fe_xCo_{1-x}]_{33.3}Zr_{66.7}$ glasses. Another important parameter contributing to the glass-forming ability of a glass is the excess negative enthalpy of mixing [23]. A simple calculation using Miedema's method [24] shows that Co-Zr alloys have a larger negative enthalpy of mixing than Fe-Zr alloys indicating the higher stability of cobalt-rich compositions. All in all, the values of T_x at the end-point composition of the Fe-Co-Zr ternary system are in agreement with those of previous work (see Table 3.2).

An increasing trend in $|\Delta H_c|$ with increasing iron content is observed in

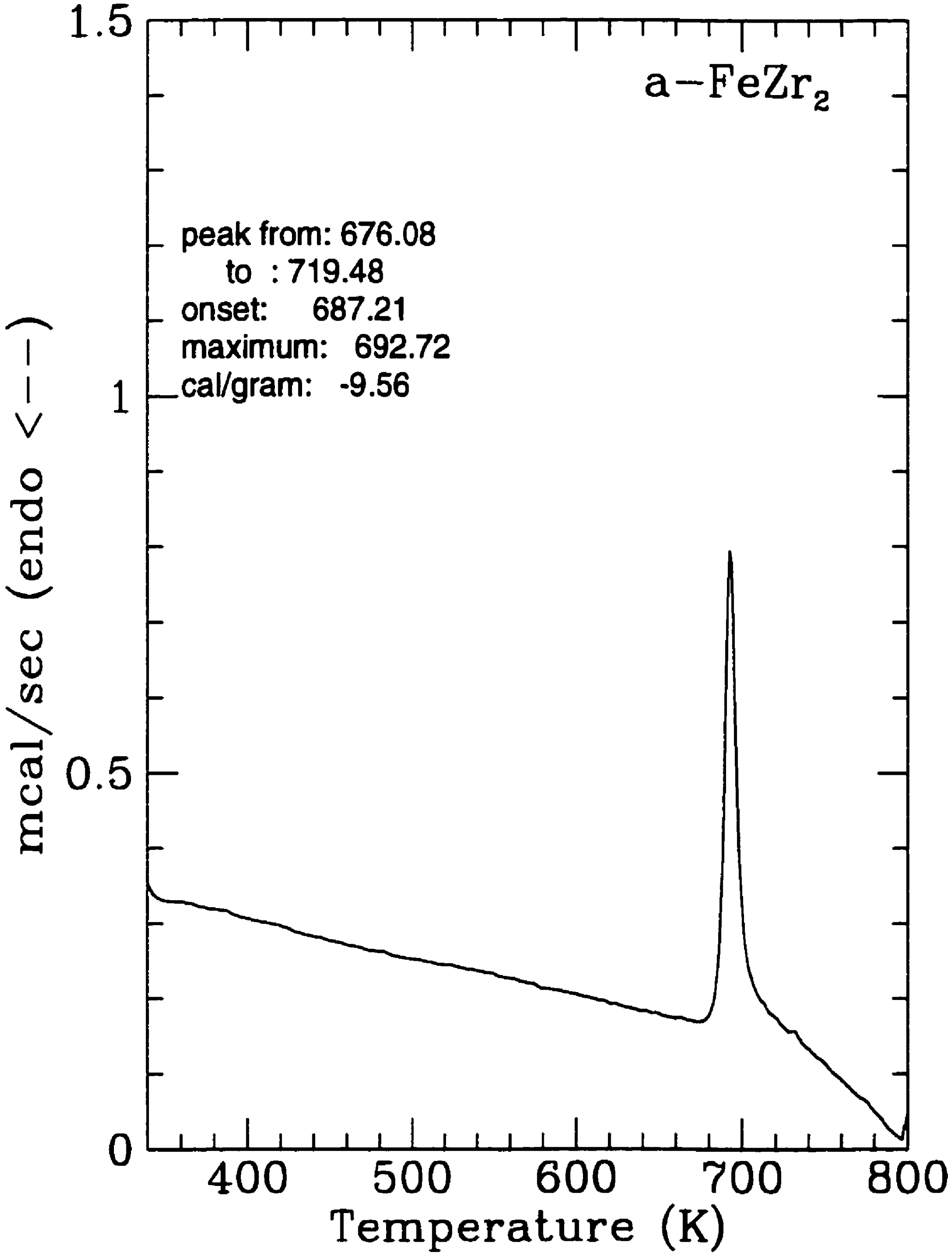

Figure 3.9: Typical DSC thermogram showing the crystallization for the as-made $(Fe_xCo_{1-x})_{33.3}Zr_{66.7}$ $(0.3 \leq x \leq 1)$ metallic glasses.

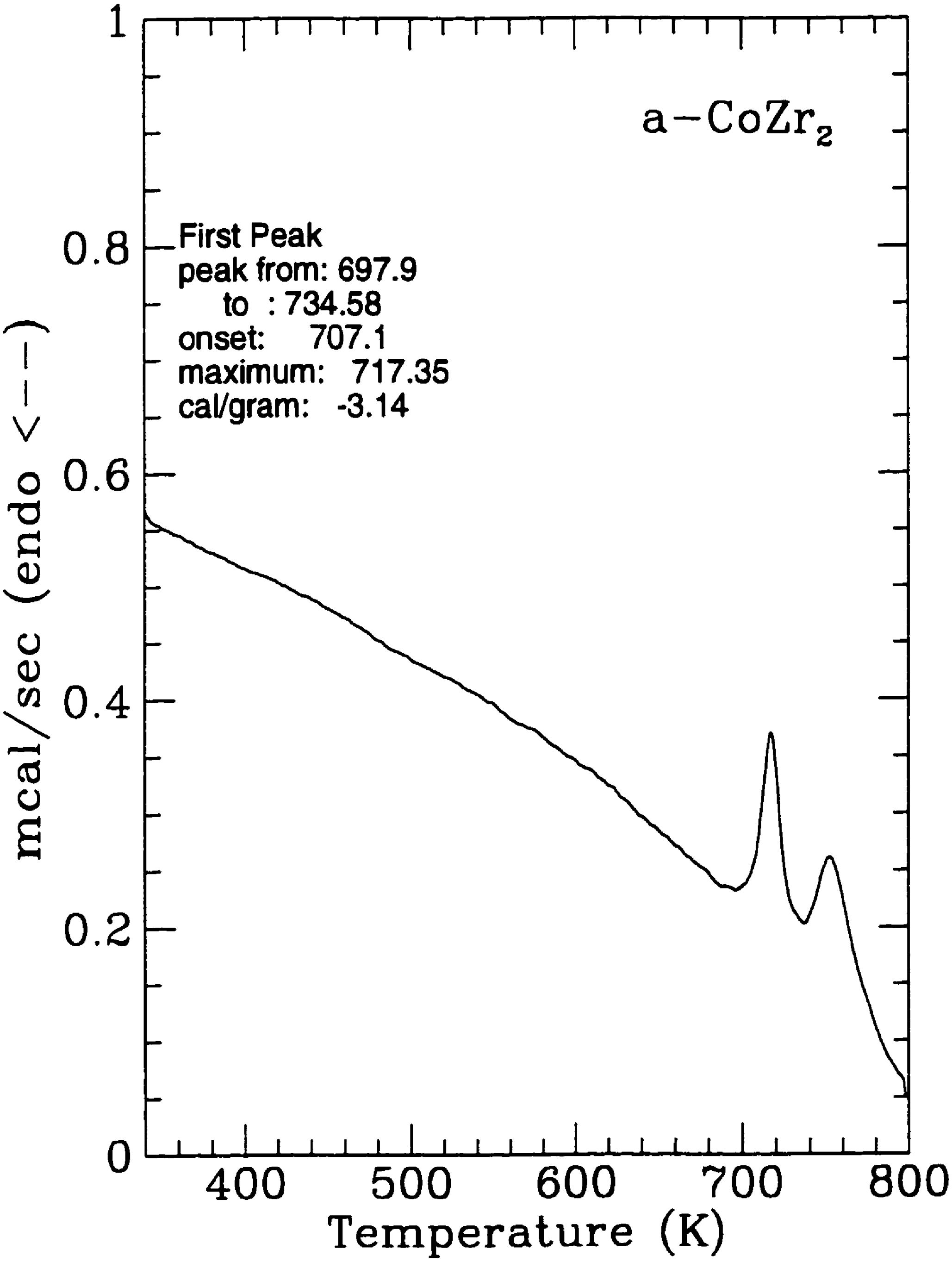

Figure 3.10: A DSC trace of the crystallization behaviour of *a*-$Co_{33.3}Zr_{66.7}$. The two exothermic peaks correspond to two transitions: the first, from the amorphous state to the metastable *fcc* phase; the second, from the *fcc* to that of the stable *bct* phase.

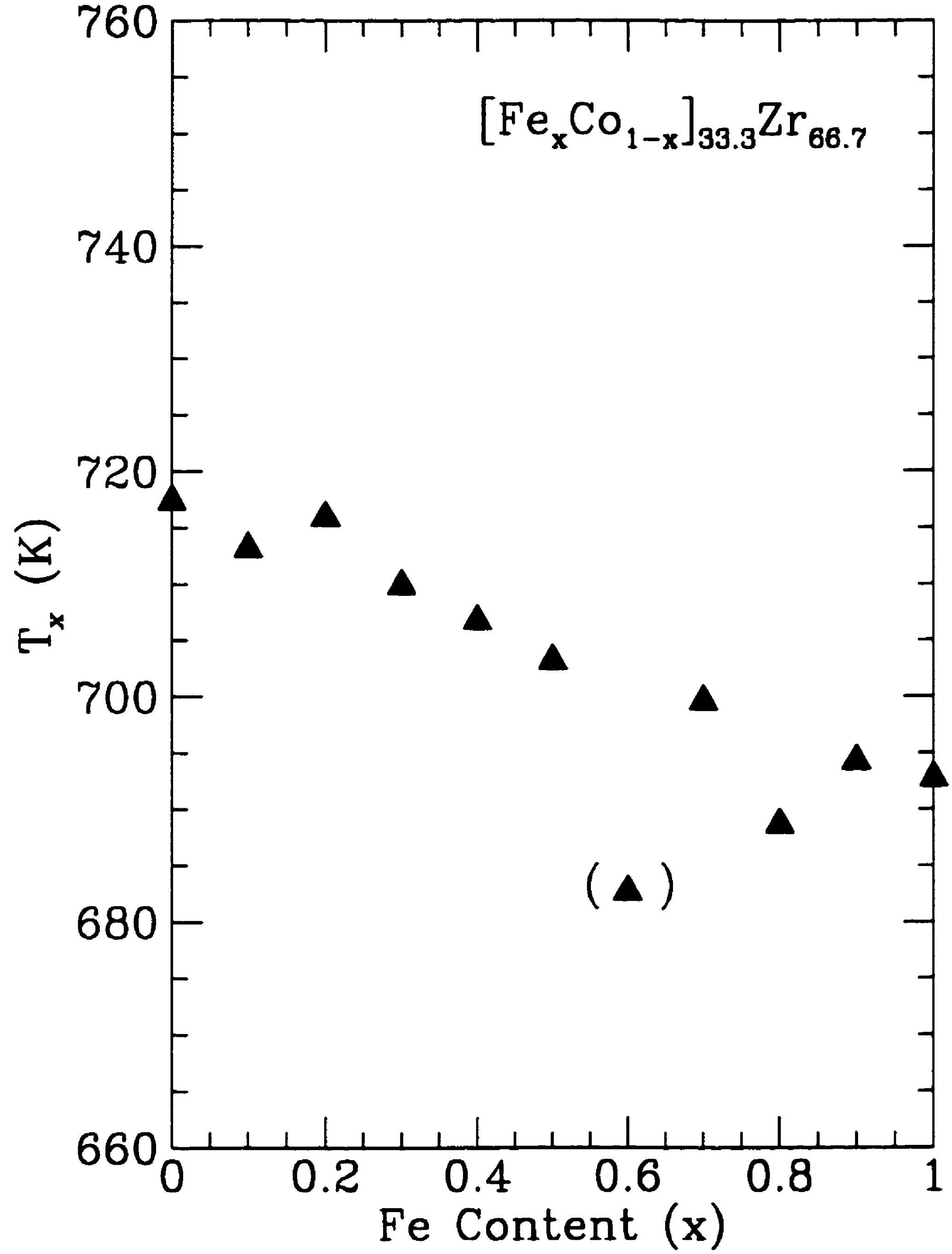

Figure 3.11: Crystallization temperatures (T_x) obtained from the DSC scans of the $(Fe_xCo_{1-x})_{33.3}Zr_{66.7}$ ribbons.

ALLOY	T_{fcc} (K)	T_{bct} (K)	d (g/cm^3)	ρ(300 K) ($\mu\Omega$ cm)
$FeZr_2$	680 [25]	1035* [25]	6.86 [26]	167 [26]
$CoZr_2$	705 [27]	785 [27]	7.12 [28]	176 [28]

Table 3.2: Previously measured values of crystallization temperatures (T_{fcc} and T_{bct}), density (d), and resistivity (ρ(300 K)) are presented in this table. The crystallization temperatures are from DSC measurements at 10 K/min (* from resistivity).

Fig. 3.12. (Note that the negative value of ΔH_c indicates that the crystallization process is exothermic. The DSC was set to record exothermic peaks as maxima and endothermic ones as minima.) The slight scatter in the data may be due to the difficulty in determining the temperature limits of the crystallization peak. The difficulty arises from the fluctuations of the DSC instrument which appear as a curved baseline. This curved baseline makes it somewhat hard to determine precisely the onset and end of the transformation.

Once again, a discrepancy for $[Fe_{0.6}Co_{0.4}]_{33.3}Zr_{66.7}$, this time in the value of ΔH_c, is noticeable. In general, the behaviour of ΔH_c for this pseudo-binary system is consistent with previous work [29,30]. ΔH_c is essentially the free energy difference between the amorphous and crystalline states. A larger $|\Delta H_c|$ for iron-rich compositions may indicate the relative stability of the crystalline phase. Indeed, the *fcc* phase of $FeZr_2$ is more stable than that of $CoZr_2$ as indicated by their transformation temperatures to the stable tetragonal phase, T_{bct}, listed in Table 3.2. To calculate ΔH_c and its composition dependence is not straightforward and may require the

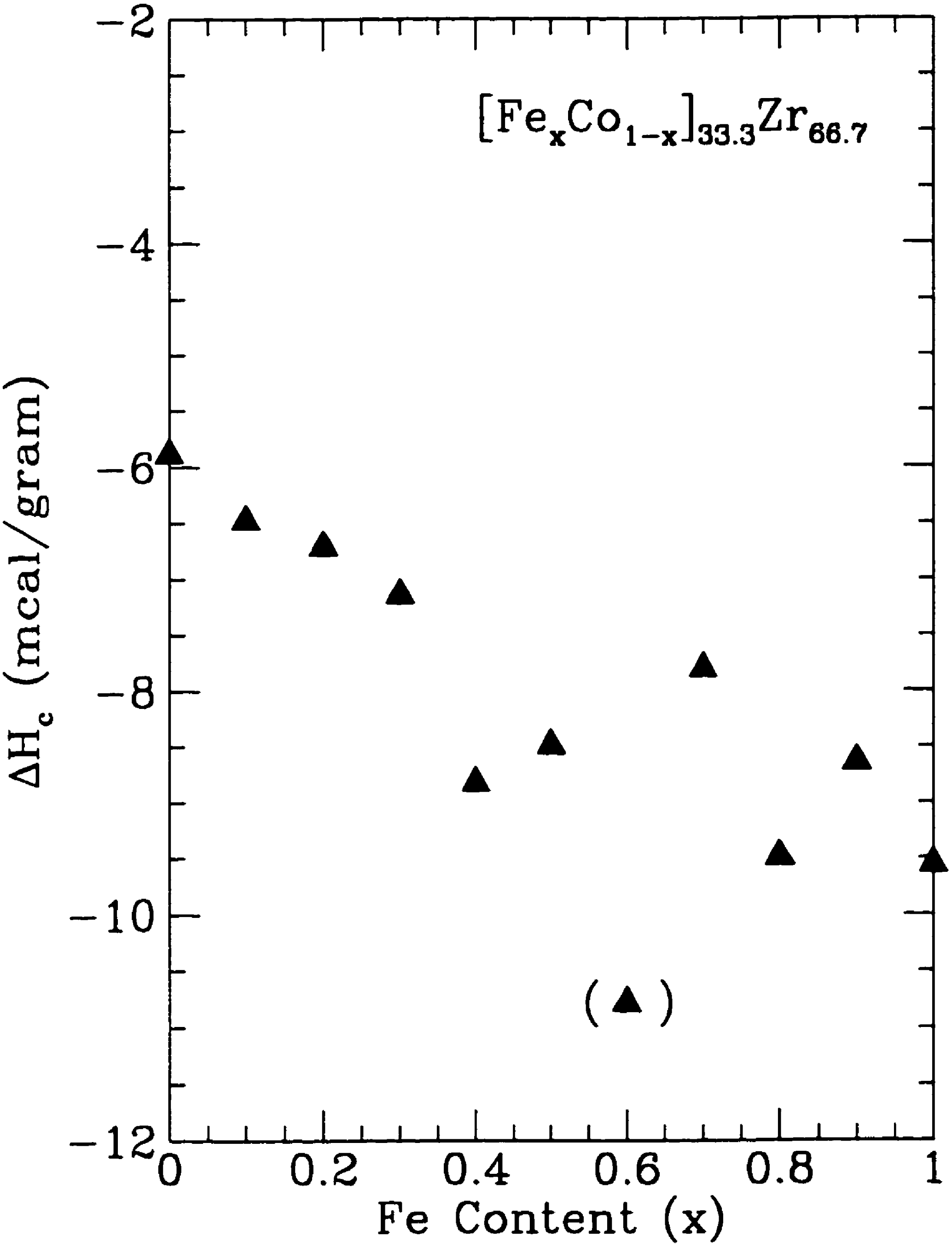

Figure 3.12: Heats of crystallization (ΔH_c) of a-(Fe$_x$Co$_{1-x}$)$_{33.3}$Zr$_{66.7}$ plotted against the nominal iron content (x).

construction of the metastable ternary phase diagram using a CALPHAD-type calculation.

3.2 Room-Temperature Resistivity

The room-temperature electrical resistance of the $[\mathrm{Fe}_x\mathrm{Co}_{1-x}]_{33.3}\mathrm{Zr}_{66.7}$ metallic glasses was measured using a four-terminal dc technique as discussed in Section 2.4.1. In order to make a comparison among the samples, these resistances had to be converted to electrical resistivities. Resistivity is usually determined by calculation from the measured resistance R of samples having known length l and uniform cross-sectional area A:

$$\rho = \frac{RA}{l} \tag{3.6}$$

To overcome the difficulties which arise when measuring the thickness of the ribbon (which may not be uniform throughout its whole length) by a micrometer, the resistivities were in fact determined from the measured resistance R, length l, mass m, and mass density d:

$$\rho = \frac{Rm}{l^2 d} \tag{3.7}$$

The densities needed to convert the resistances to resistivities were measured by Archimedes' principle as discussed in Section 2.3. Table 3.3 lists ρ and d at room temperature. Although the values for the the end-point compositions are in relative agreement with those given in Table 3.2, the small differences are probably caused by the subtle complexities involved in determining the densities just mentioned. Slightly inaccurate mass measurements, most likely owing to air drafts present at the location of the balance, are propagated by the subsequent calculations. The presence of small air bubbles attached to the ribbons is also a problem, and is the

$a\text{-}[\mathrm{Fe}_x\mathrm{Co}_{1-x}]_{33.3}\mathrm{Zr}_{66.7}$		
Fe CONTENT x (nominal)	DENSITY d ($\pm$ 0.05 g/cm^3)	RESISTIVITY ρ(300 K) ($\pm$ 0.8 $\mu\Omega$ cm)
0	6.97	173.7
0.1	6.52	183.7
0.2	6.82	175.6
0.3	6.83	174.4
0.4	6.53	179.7
0.5	6.91	171.2
0.6	6.74	169.6
0.7	6.85	172.1
0.8	6.70	172.1
0.9	6.72	170.9
1.0	6.89	159.8

Table 3.3: Measured values of the density, d, and room-temperature resistivities, $\rho(300\ \mathrm{K})$, for the $a\text{-}\mathrm{Fe}_x\mathrm{Co}_{1-x}\mathrm{Zr}_2$ ribbons.

principal cause for lower densities. This appears to be the case for $x = 0.1$ and 0.4 giving rise to somewhat large values for ρ.

The room-temperature resistivity of the a-$[Fe_xCo_{1-x}]_{33.3}Zr_{66.7}$ samples versus the iron content are plotted in Fig. 3.13. The data suggest that a slight decrease in $\rho(300K)$ occurs as a function of iron content.

3.3 Temperature Dependence of the Resistivity

The temperature dependence of the electrical resistivity $\rho(T)$, in the range from 80 K to 300 K, was studied for both the amorphous and crystalline $[Fe_xCo_{1-x}]_{33.3}Zr_{66.7}$ alloy systems.

According to the generalized Faber-Ziman theory, the resistivity may be expressed by the equation:

$$\rho = exp[-2W(T)](\rho_0 + \Delta\rho) \tag{3.8}$$

where ρ_0 is the residual resistivity at 0 K, $\Delta\rho$ is the contribution due to inelastic electron-phonon interaction, and the exponential term is the Debye-Waller factor [5]. At low temperatures, not below 20 K, expansion of the Debye-Waller factor yields

$$\rho = 1 - \beta T^2 \tag{3.9}$$

This temperature dependence of the resistivity is characteristic of metallic glasses with sp electrons at the Fermi energy, E_F. Moreover, it is believed to be due to the interaction of the sp conduction electrons with the "Faber-Ziman lattice" vibrations (i.e., atomic vibrations) [7]. Figure 3.14 shows the ρ vs. T relation for the zirconium-based Fe-Co-Zr ternary glasses. The data exhibit a $(c-bT+aT^2)$-dependence which is markedly different from that predicted by the generalized Faber-Ziman theory

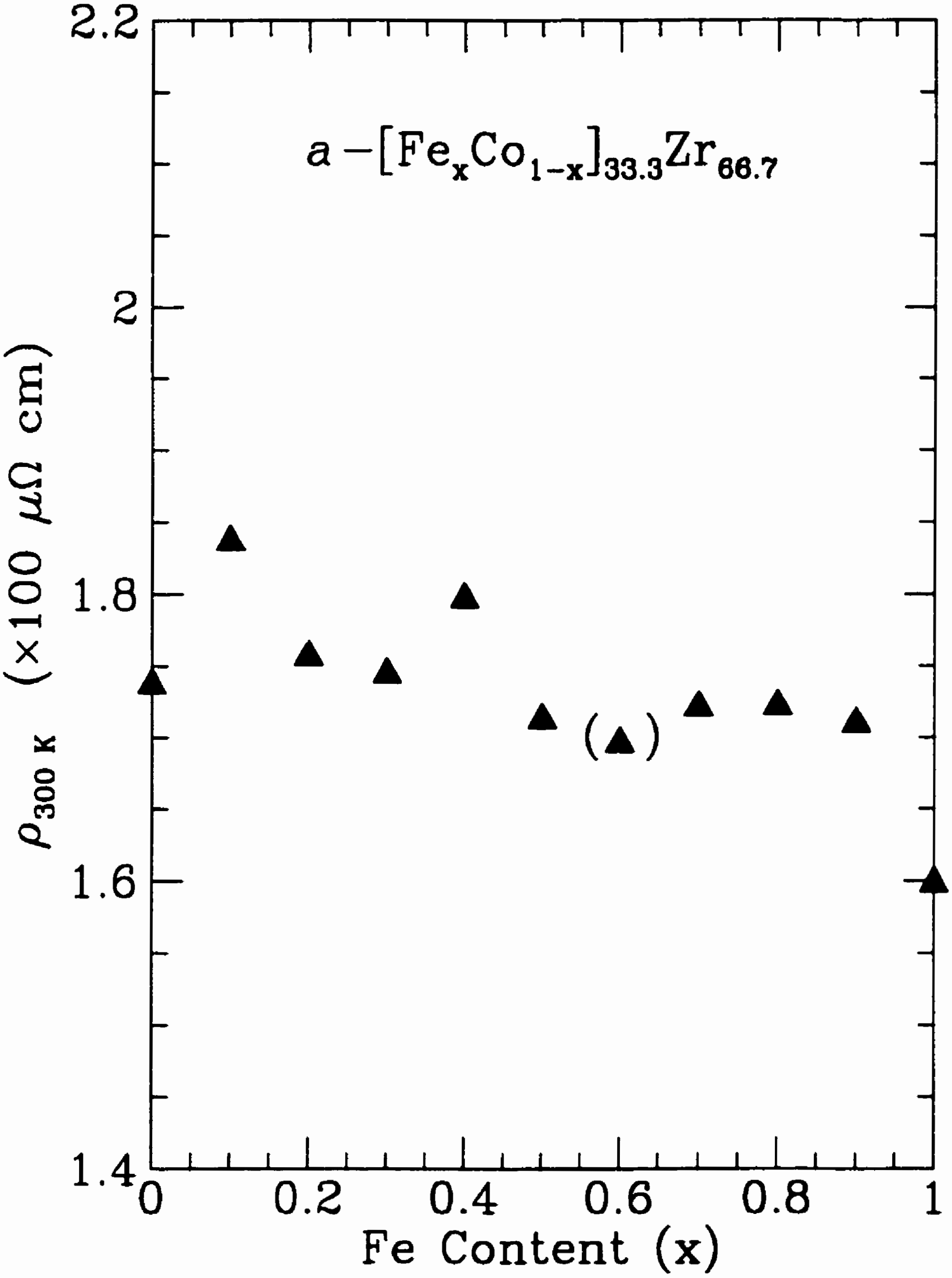

Figure 3.13: Room-temperature resistivity of a-$(Fe_xCo_{1-x})_{33.3}Zr_{66.7}$ ribbons.

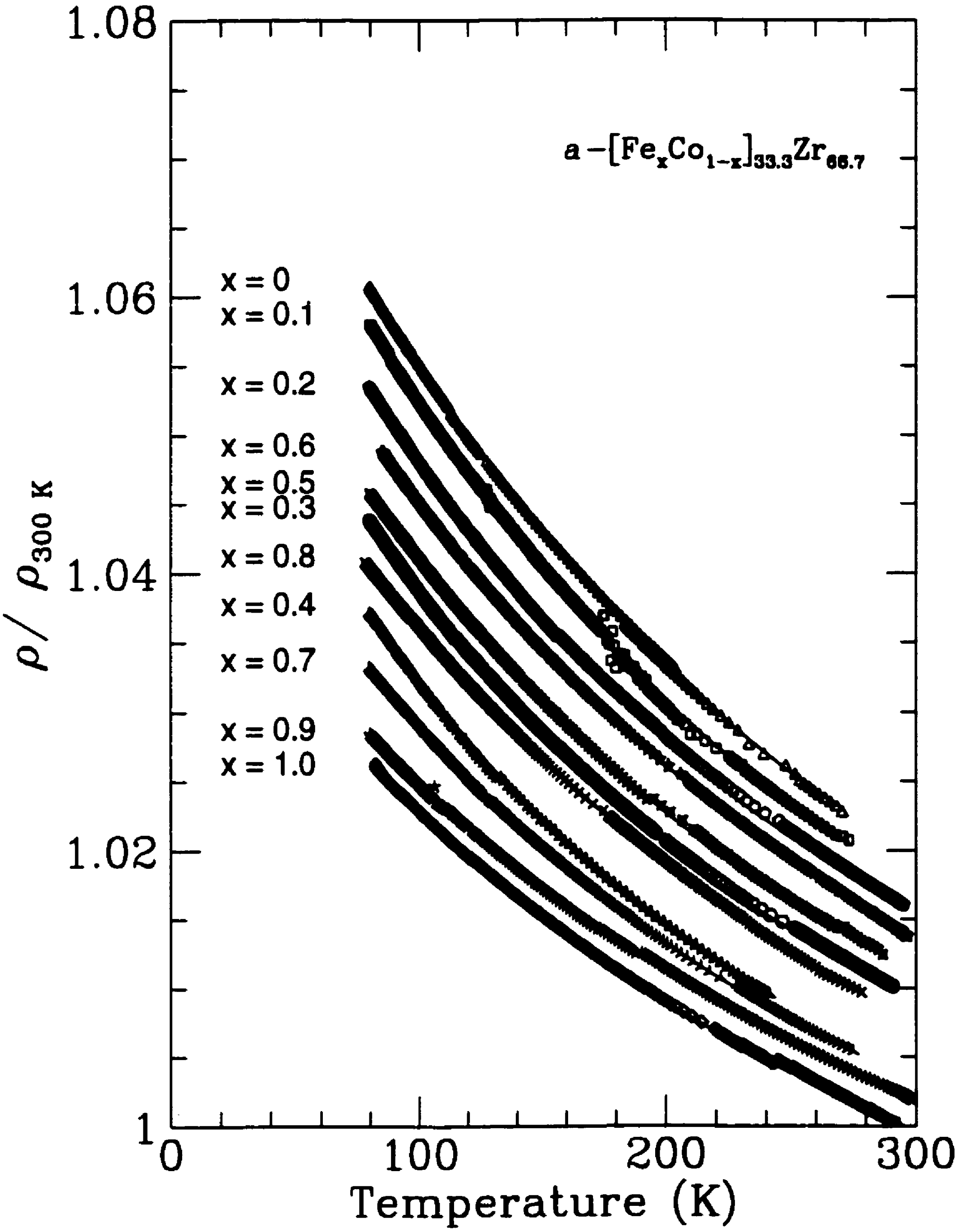

Figure 3.14: Temperature dependence of the resistivity ratio for a-$Fe_xCo_{1-x}Zr_2$. The solid curves through the data points are the quadratic fits to the data (see Section 3.3). Note that the data have been shifted for clarity.

(see Eq. (3.9)). This deviation arises in glasses, such as those studied here, which contain a significant number of d electrons at E_F [7]. For these metallic glasses, the d-electron contribution to the scattering mechanism needs to be considered; the generalized Faber-Ziman theory is no longer valid.

It has been proposed by Mizutani [7] that this unique temperature dependence of the resistivity in the range 30-300 K is given by the following empirical equation

$$\frac{\rho}{\rho_{300K}} = A + Bexp(\frac{-T}{\Delta}) \tag{3.10}$$

where A, B, and Δ are the fitting parameters. The results of the least-squares fitting to Eq. (3.10) for the resistivity data of the Fe-Co-Zr glass system are shown in Fig. 3.15. The data conform well to the fitted exponential throughout the entire temperature range studied, i.e., from 80 K to 300 K.

Earlier work on electron transport properties of metallic glasses [31] suggests a correlation between the characteristic temperature Δ (which is considered to be an indication of the interaction with the "lattice vibration") and the Debye temperature θ_D: an increase in θ_D corresponds to an increase in Δ. A plot of Δ against the iron content for the a-$[Fe_xCo_{1-x}]_{33.3}Zr_{66.7}$ system studied here is found in Fig. 3.16. Clearly, the characteristic temperature Δ fluctuates about 220 K. The values of Δ compare well with the value of θ_D for a-$Fe_{33}Zr_{67}$ ($\theta_D = 210$ K) given in Ref. [30]. Any dependence of Δ on the iron content of the ternary compounds is not obvious. The value of the parameter A is approximately unity and does not show any dependence on the iron content of the samples. On the other hand, as shown in Fig. 3.17, B seems to decrease as the amount of iron decreases. Mizutani [7] suggests that the parameter B is a function of the electronic specific heat coefficient, γ, and shows that B increases as the density of states at E_F increases – thus, indicating that a high density of states involving the d-electrons is of importance. In fact, the values

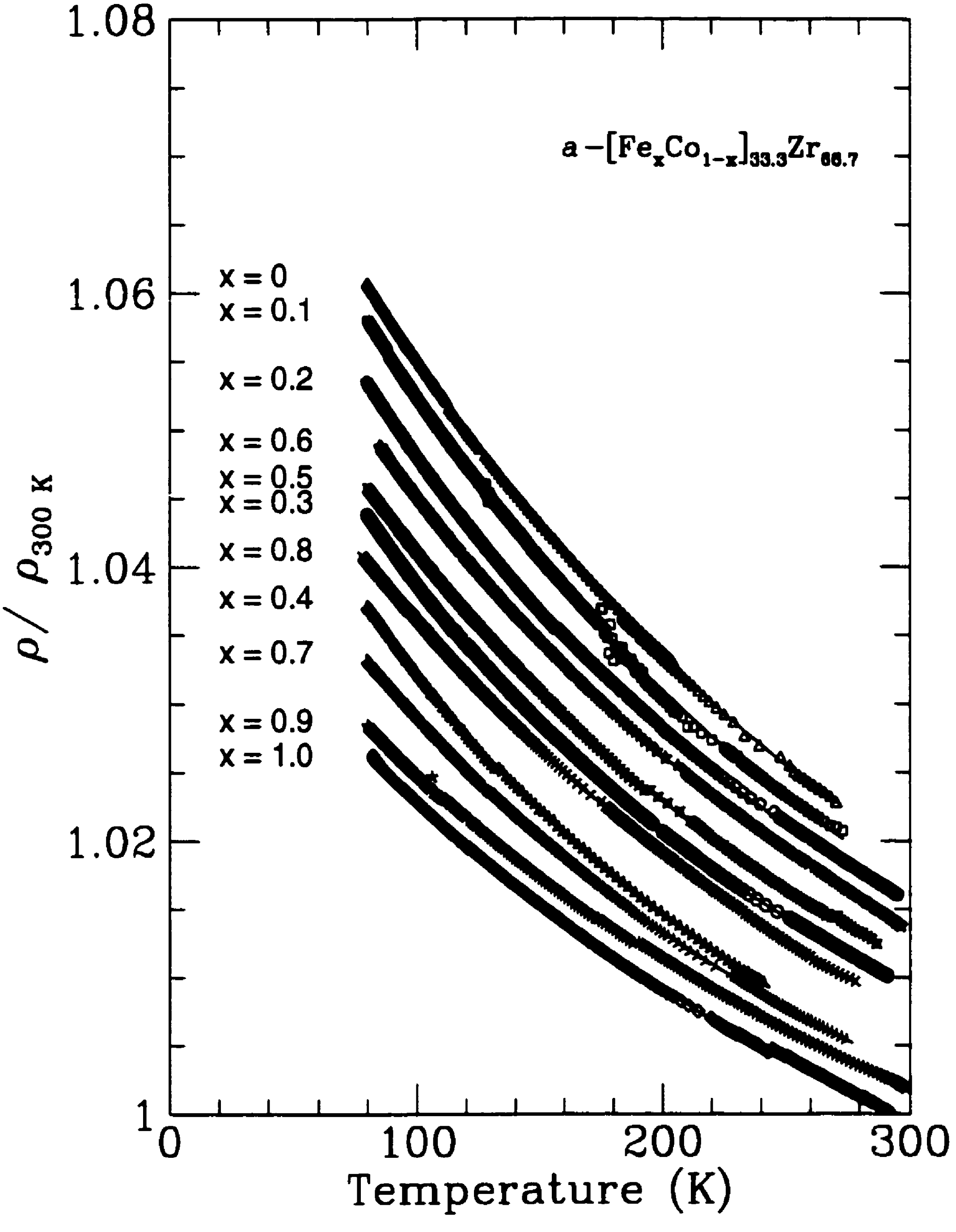

Figure 3.15: Temperature dependence of the resistivity ratio for a-$Fe_xCo_{1-x}Zr_2$. The solid curves through the data points are the exponential fits to the data (see Eq. (3.10)). Note that the data have been shifted for clarity.

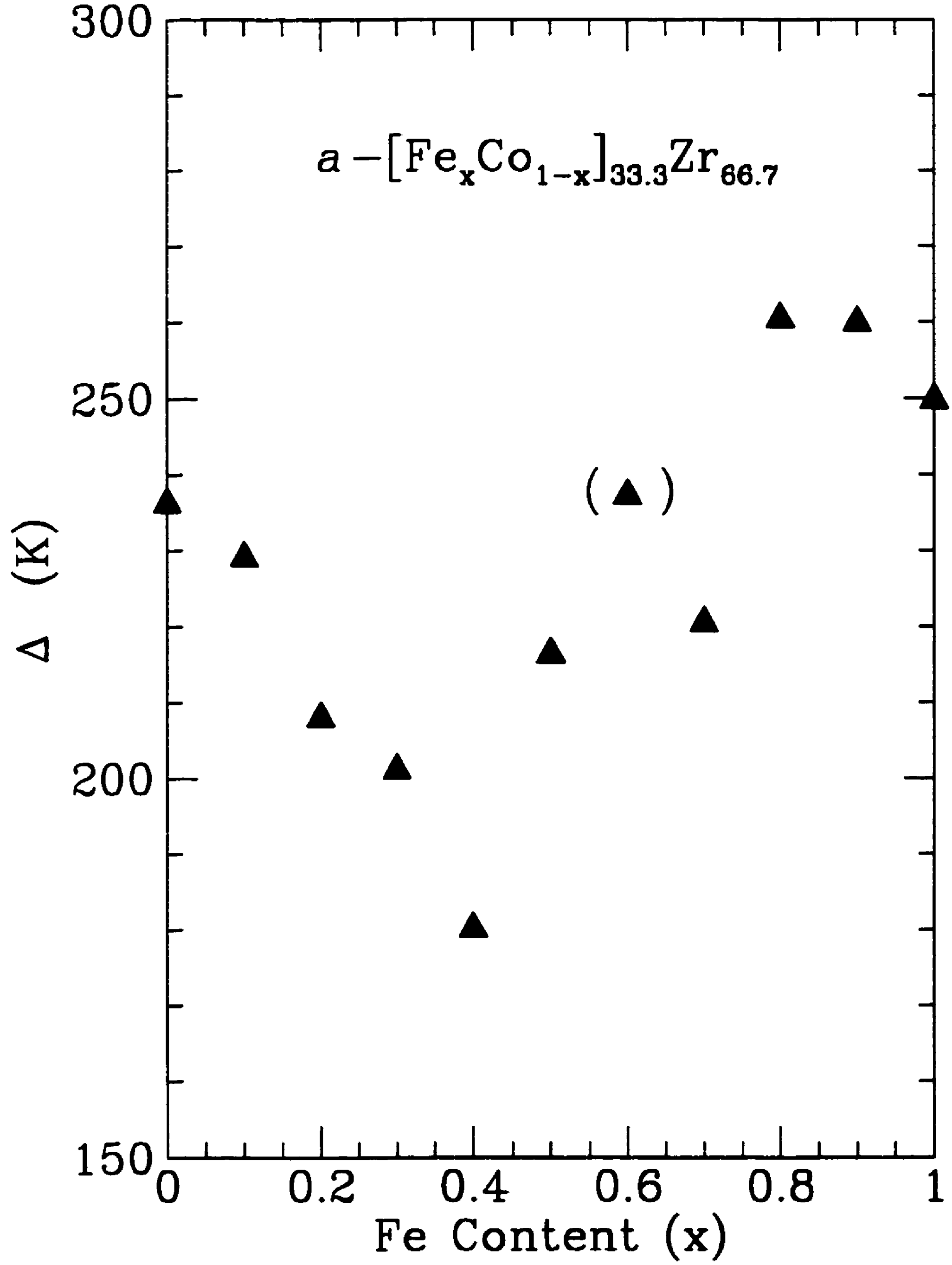

Figure 3.16: Plot of Δ versus iron content x for the Fe-Co-Zr glasses. Recall that Δ is a parameter of the exponential fit (see Eq. (3.10) in the text).

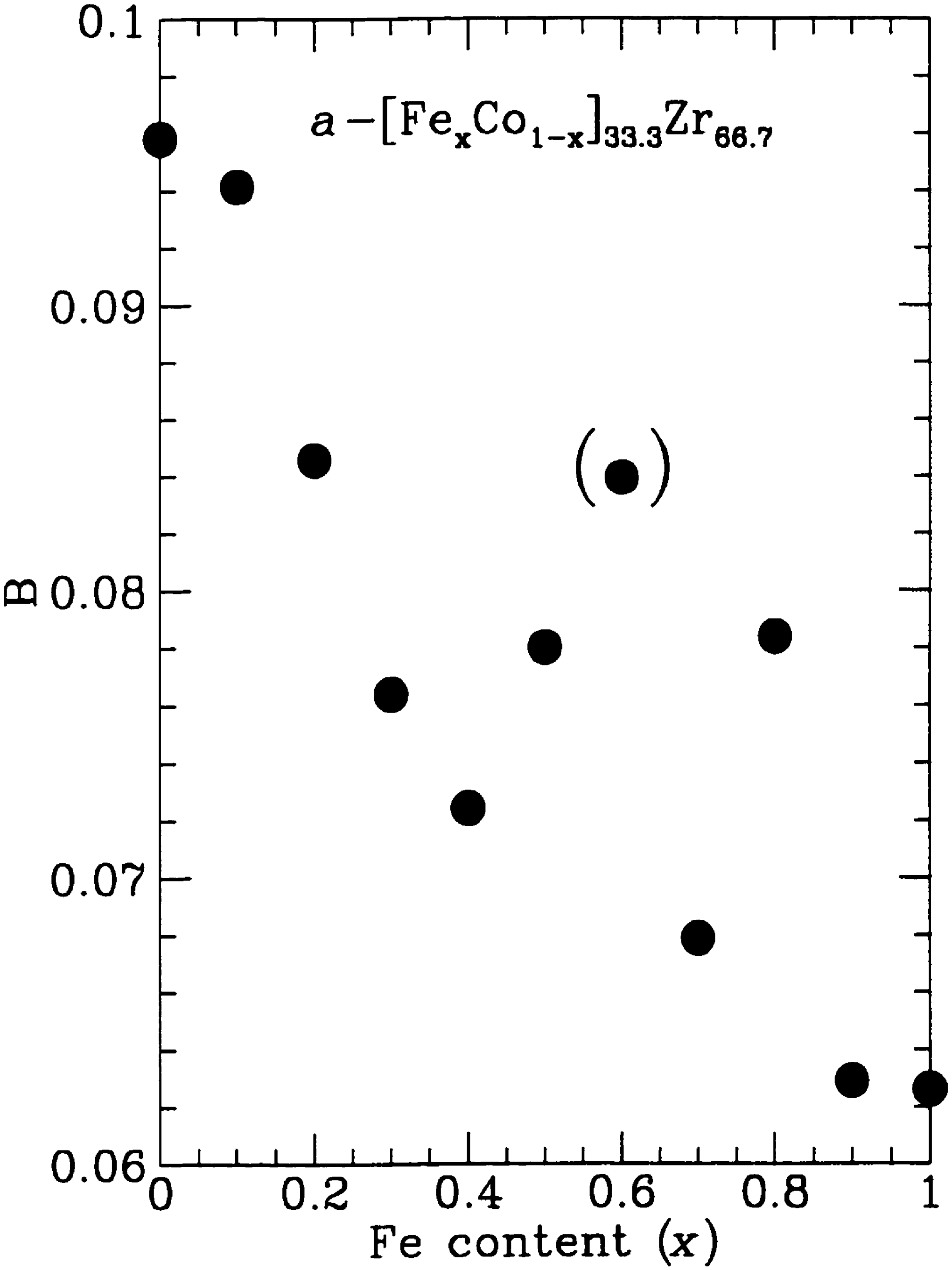

Figure 3.17: Plot of B versus iron content x for the Fe-Co-Zr glasses. Recall that B is a parameter of the exponential fit (see Eq. (3.10) in the text).

of B obtained here were of the same order of magnitude as those shown in Ref. [7].

The temperature coefficient of the resistivity, α, is yet another means of characterizing metallic glasses. It is defined as $(1/\rho)(d\rho/dT)$ from the slope of the ρ-T curve in the range 200-300 K. A negative α has been observed in many non-magnetic metallic glassses [5,28]. In fact, a negative α and ρ(300 K) in the range 150-200 $\mu\Omega$ cm are typical of many metal-metal metallic glasses [5,7]. A plot of α against the iron content of a-$[\mathrm{Fe}_x\mathrm{Co}_{1-x}]_{33.3}\mathrm{Zr}_{66.6}$ is shown in Fig. 3.18. Indeed, as expected, α is negative for the metal-metal pseudo-binary system studied here. Furthermore, Fig. 3.18 indicates a decreasing tendency in $|\alpha|$ with increasing iron content x. The observation that, as the cobalt content is increased, ρ increases (as shown in Fig. 3.13) together with the increasingly more negative values of α (as shown in Fig. 3.18) are consistent with the well-known Mooij correlation [32] which states that for disordered systems containing d-electrons: (i) for $\rho \geq 150$ $\mu\Omega$ cm, α is negative, and (ii) the larger the value of ρ, the larger the value of $|\alpha|$.

The electrical resistivity data of the crystalline Fe-Co-Zr system are displayed in Fig. 3.19. A $(c - bT + aT^2)$ – dependence similar to their amorphous counterparts is evident. This suggests the possibility that the amorphous and crystalline systems share a common scattering mechanism in this temperature range. This behaviour of the resistivity is atypical of most crystals. Figure 3.20 explicitly shows the negative values of α obtained for the crystalline system. This unexpected behaviour may indicate a heavily disordered crystalline structure and merits further study.

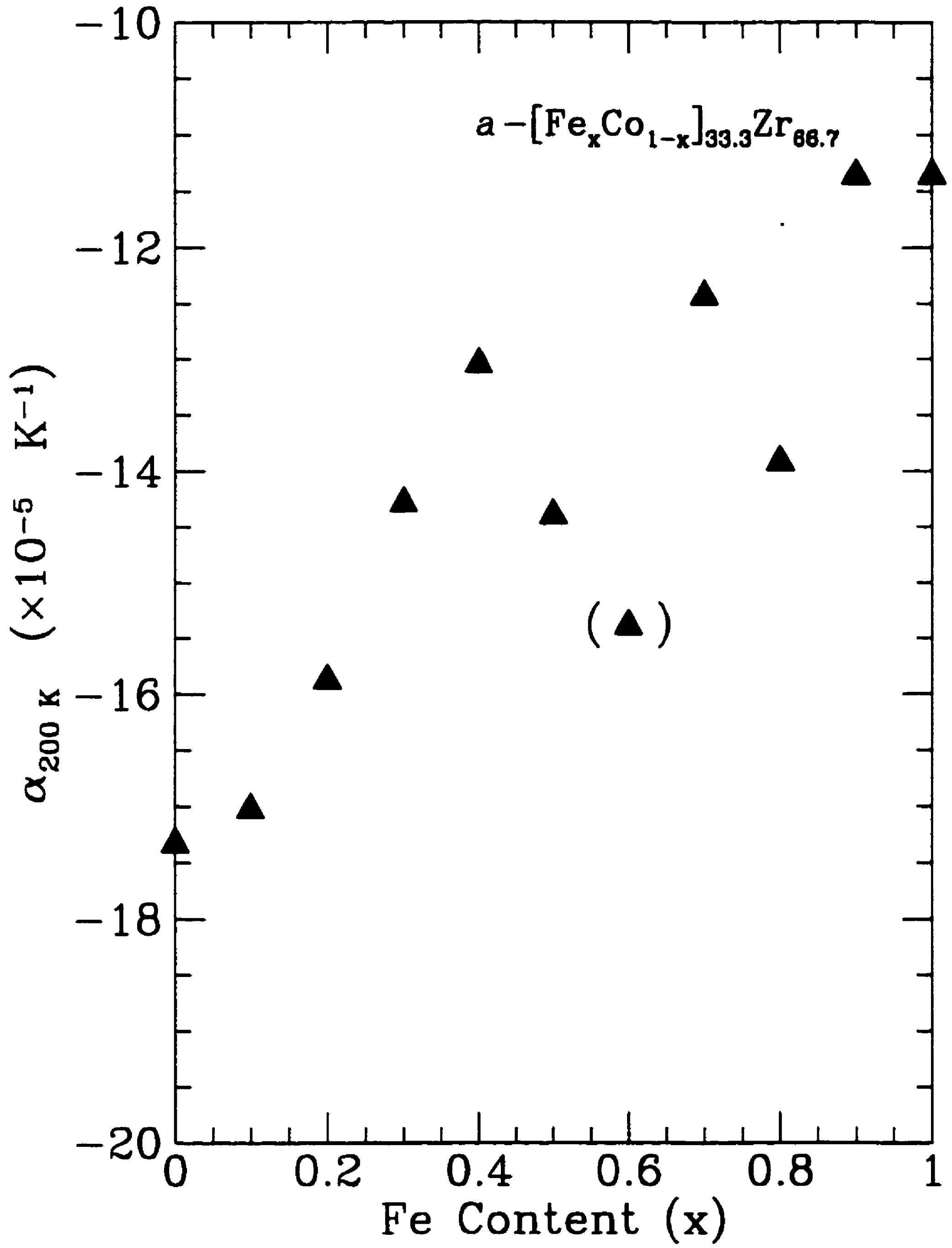

Figure 3.18: Plot of the temperature coefficient of resistivity, α, versus the iron content x for the Fe-Co-Zr glasses. Note that α is evaluated at 200 K.

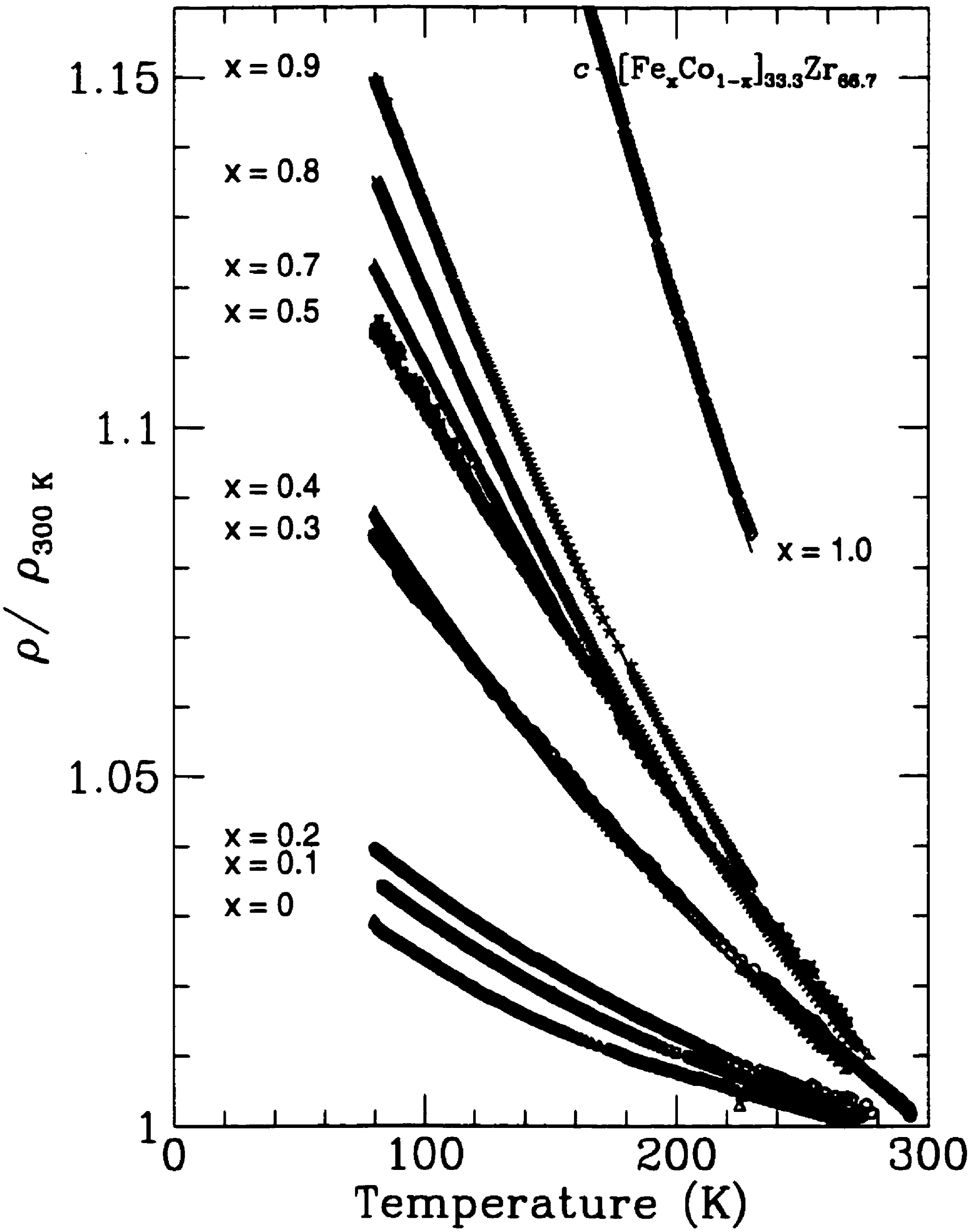

Figure 3.19: Temperature dependence of the resistivity for c-Fe$_x$Co$_{1-x}$Zr$_2$. The solid curves are the quadratic fits to the data.

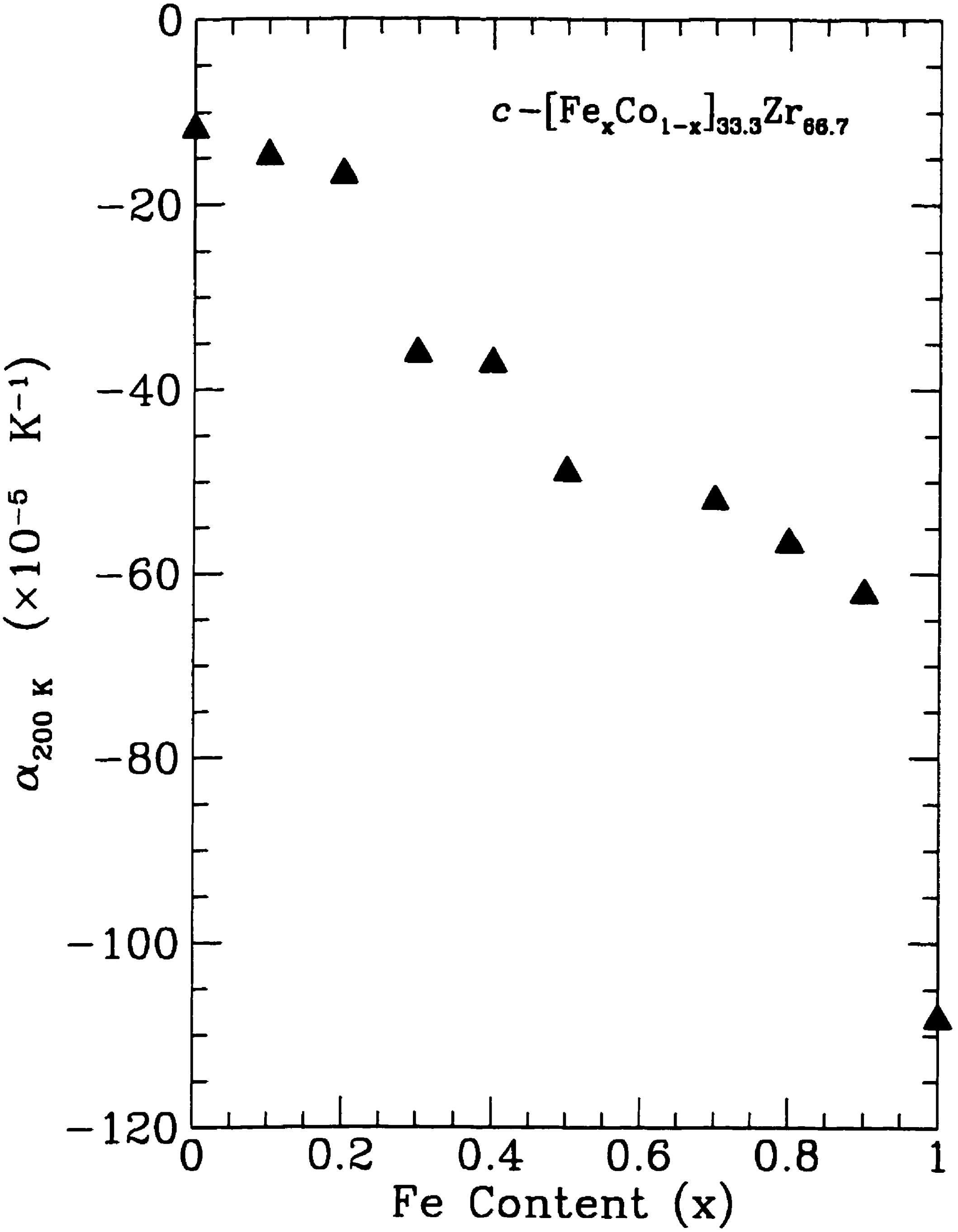

Figure 3.20: Plot of the temperature coefficient of resistivity, α, versus the iron content x for c-$Fe_xCo_{1-x}Zr_2$. Note that α is evaluated at 200 K.

Chapter 4

Conclusions

In this thesis, the electronic contribution to the resistivity and its temperature dependence was investigated for amorphous and crystalline $[Fe_xCo_{1-x}]_{33.3}Zr_{66.7}$ $(0 \leq x \leq 1)$ alloys.

As set out to do, samples of $[Fe_xCo_{1-x}]_{33.3}Zr_{66.7}$ metallic glasses were prepared using the single-roller melt-spinning technique and characterized by means of electron-microprobe analysis, X-ray diffraction, and differential scanning calorimetry. The amorphous samples were found to be chemically homogeneous, and free of crystalline phases. Moreover, the first crystallization product for all the compositions was the *fcc* $NiTi_2$-type structure as desired. Furthermore, as the amount of cobalt was increased in the $[Fe_xCo_{1-x}]_{33.3}Zr_{66.7}$ glasses, a small increase in T_x (i.e., stability) was observed. This is consistent with earlier observations [22] that the stability of a glass or its glass-forming ability increases with the atomic-size difference of its constituent elements – in this instance, the cobalt atom is slightly smaller than the iron atom.

It has been proposed by Mizutani [7] that the ρ vs. T relation for glasses which contain a significant amount of d electrons at E_F is

$$\frac{\rho}{\rho_{300K}} = A + Bexp(\frac{-T}{\Delta}) \tag{4.1}$$

For the Fe-Co-Zr glasses studied here, the exponential relation held well over the entire experimental temperature range (i.e., 80- 300 K). Values of the characteristic temperature Δ (believed to be related to the Debye temperature θ_D) were reasonable as compared with the value of θ_D for a-$Fe_{33}Zr_{67}$ ($\theta_D = 210$ K) given in Ref. [30]. The parameter B (which is related to the electronic specific heat coefficient γ) decreased as the amount of iron in the amorphous samples increased. On the other hand, the parameter A was approximately unity and did not show any dependence on composition.

The temperature coefficient of the resistivity, α, for the ternary glasses was negative (which is in accordance with previous work on similar systems [5,28]) and became increasingly negative with decreasing iron content. It was also observed that as the iron content increased, $\rho(300$ K$)$ decreased. These observations are consistent with the well-known Mooij correlation [32] for disordered systems containing d-electrons: (i) for $\rho \geq 150$ $\mu\Omega$ cm, α is negative, and (ii) the larger the value of ρ, the larger the value of $|\alpha|$.

The resistivity data for the crystalline Fe-Co-Zr system exhibited a quadratic temperature dependence of the form: $c - bT + aT^2$. In addition, the temperature coefficient of the resistivity (α) was negative. This is atypical of most crystals and may indicate a heavily disordered crystalline system.

Future work in this area will include a study of the spin fluctuation phenomenon present at low temperatures in iron containing glasses, superconducting properties and quantum corrections to the conductivity. A detailed comparison between the electron transport properties in amorphous and crystalline systems with similar compositions will also be studied in an attempt to explain the unusual electron transport properties of the crystallized alloys.

References

[1] T.R. Anantharaman, and C. Suryanarayana, *Rapidly Solidified Metals* (Trans Tech Publications, Brookfield, VT, 1987).

[2] Kishin Moorjani, and J.M.D. Coey, *Magnetic Glasses*, edited by S.P. Wolsky and A.W. Czanderna (Elsevier, New York, 1984).

[3] C.E. Applegate and Jack Bass, *Solid State Physics Source Book*, edited by S.P. Parker (McGraw-Hill, New York, 1988), pp. 148, 165.

[4] S.R. Elliot, *Physics of Amorphous Materials* (Longman Scientific & Technical, Essex, 1983).

[5] U. Mizutani, Prog. Mat. Sci. **28**, 97 (1983).

[6] T.E. Faber and J.M. Ziman, Phil. Mag. **11**, 153 (1965).

[7] U. Mizutani, "Systematic Studies of Electron Transport Properties of Metallic Glasses" in *Rapidly Quenched Metals V, Volume 1*, edited by S. Steeb and H. Warlimont (Elsevier, New York, 1985), p. 977.

[8] L.G. Aslamasov, and A.I. Larkin, Phys. Lett. **26A**, 238 (1968).

[9] S. Ami, and K. Maki, Phys. Rev. **B18**, 4714 (1978).

[10] S. Ami, and K. Maki, Phys. Rev. **B19**, 1403 (1979).

[11] W.L. Johnson, and C.C. Tsuei, Phys. Rev. **B13**, 4827 (1976).

[12] W.L. Johnson, C.C. Tsuei, and P. Chaudhari, Phys. Rev. **B17**, 2884 (1978).

[13] Z. Altounian, S.V. Dantu, and M. Dikeakos, Phys. Rev. **B49**, 8621 (1994).

[14] R. Zallen, *The Physics of Amorphous Solids* (John Wiley & Sons, New York, 1983).

[15] Y. Nishi, T. Morohoshi, M. Kawakami, K. Suzuki, and T. Masumoto, *Proc. of the 4th Int. Conf. on Rapidly Quenched Metals, Volume 1*, edited by T. Masumoto and K. Suzuki (Japan Institute of Metals, Sendai, 1982), p. 111.

[16] S. Brauer, *PhD Thesis* (McGill University, Montreal, 1992).

[17] J.L. McNaughton, and C. T. Mortimer, *Differential Scanning Calorimetry* (Perkin-Elmer Corporation, Norwalk, 1975).

[18] TRA-DUCT 2902 Conductive Silver Epoxy Adhesive, *J.B. EM Services Inc.* (Dorval, Quebec H9R 4S8).

[19] R. Brüning, *PhD Thesis* (McGill University, Montreal, 1990).

[20] General X-ray Structural Analysis Software developed by E.V. Shelekhov at the *Department of X-ray Structural Analysis and Metal Physics, Moscow Steel and Alloys Institute.*

[21] P. Villars, and L.D. Calvert, *Pearson's Handbook of Crystallographic Data for Intermetallic Phases, Volumes 2 & 3* (American Society for Metals, Metals Park OH, 1986).

[22] D.E. Polk, and B.C. Giessen, *Metallic Glasses* (American Society for Metals, Metals Park OH, 1978), p. 1.

[23] P. Zielinski, J. Ostalek, M. Kijek, and H. Matyja, *Proceedings of the Third International Conference on Rapidly Quenched Metals, Volume 1*, edited by B. Cantor (The Metals Society, London, 1978), p. 337.

[24] A.R. Miedema, P.F. de Châtel, and F.R. DeBoer, Physica **100**, 1 (1980).

[25] Z. Altounian, C.A. Volkert, and J.O. Ström-Olsen, J. Appl. Phys. **57**, 1777 (1985).

[26] M. Sabouri-Ghomi, *MSc Thesis* (McGill University, Montreal, 1995).

[27] Z. Altounian, R.J. Shank, and J.O. Ström-Olsen, J. Appl. Phys. **58**, 1192 (1985).

[28] Z. Altounian, and J.O. Strom-Olsen, Phys. Rev. B**27**, 4149 (1983).

[29] S.V. Dantu, *MSc Thesis* (McGill University, Montreal, 1989).

[30] A.LeR. Dawson, *PhD Thesis* (McGill University, Montreal, 1994).

[31] U. Mizutani, "Electron Transport Properties of Non-magnetic Metallic Glasses" in *Rapidly Quenched Metals 6, Volume 3*, edited by R.W. Cochrane and J.O. Ström-Olsen (Elsevier, New York, 1988), p. 165.

[32] J.M. Mooij, Phys. Stat. Solidi. A**17**, 521 (1973).